

Southern Methodist University

SMU Scholar

Civil and Environmental Engineering Theses and
Dissertations

Civil Engineering and Environmental
Engineering

Fall 2018

Flexural Rigidity Estimation Using Noisy Static Influence Lines

Yasha Hajzeinalibiouki

Southern Methodist University, yasha.zeinali@gmail.com

Follow this and additional works at: https://scholar.smu.edu/engineering_civil_etds



Part of the [Structural Engineering Commons](#)

Recommended Citation

Hajzeinalibiouki, Yasha, "Flexural Rigidity Estimation Using Noisy Static Influence Lines" (2018). *Civil and Environmental Engineering Theses and Dissertations*. 1.

https://scholar.smu.edu/engineering_civil_etds/1

This Dissertation is brought to you for free and open access by the Civil Engineering and Environmental Engineering at SMU Scholar. It has been accepted for inclusion in Civil and Environmental Engineering Theses and Dissertations by an authorized administrator of SMU Scholar. For more information, please visit <http://digitalrepository.smu.edu>.

FLEXURAL RIGIDITY ESTIMATION USING NOISY STATIC INFLUENCE LINES

Approved by:

Dr. Brett A. Story
Assistant Professor, Civil and Environmental Engineering

Dr. Khaled Abdelghany
Professor, Civil and Environmental Engineering

Dr. Dinesh Rajan
Department Chair and Professor, Electrical Engineering

Dr. Usama El Shamy
Associate Professor, Civil and Environmental Engineering

Dr. Ali Heydari
Assistant Professor, Mechanical Engineering

FLEXURAL RIGIDITY ESTIMATION USING NOISY STATIC INFLUENCE LINES

A Dissertation Presented to the Graduate Faculty of

The Bobby B. Lyle School of Engineering

Southern Methodist University

in

Partial Fulfillment of the Requirements

for the degree of

Doctor of Philosophy in Civil Engineering

With an Emphasis in

Structural Engineering

by

Yasha Zeinali

M.Sc. Structural Engineering, Amirkabir University of Technology, 2014

B.Sc. Civil Engineering, Amirkabir University of Technology, 2011

December 15th, 2018

Zeinali, Yasha B.Sc. Civil Engineering, Amirkabir University of Technology, 2011
 M.Sc. Structural Engineering, Amirkabir University of Technology, 2014

Flexural Rigidity Estimation Using Noisy Static Influence Lines

Advisor: Dr. Brett A. Story

Doctor of Philosophy in Civil Engineering conferred December 15th, 2018

Thesis completed December 15th, 2017

Society depends on critical infrastructure to support everyday activities. Even as critical components of civil infrastructure approach and exceed their design lives, demand on these structures continues to increase. In light of the need for managing aging infrastructure, several opportunities exist for research that can aid infrastructure managers in significant the challenge of detecting, classifying, and mitigating structural impairments.

This dissertation presents a novel framework for impairment detection through the capture and utilization of deformation influence lines for flexural rigidity estimation on Euler-Bernoulli beams. In this research study, mechanical theory, a computer-vision algorithm, and multiple numerical methods are integrated to demonstrate the feasibility of the FRE method. The theoretical relationship between the second derivative of the deformation influence line and the flexural rigidity of a beam is developed. This formulation allows for both the location and quantification of damage directly from either beam deflections or rotations caused by moving loads. To overcome the challenges arising from noisy measurements that occur in practical applications, three numerical methods are proposed and compared: Moving Window (MW), Least-mean Square Error (LSQ), and Tikhonov Regularization (TR). In the analytical studies, the performance of the proposed

methods in different combinations of noise level in the measurement and number of measurements is studied. Additionally, a camera-based deformation measurement method is presented and evaluated to measure deflection or rotation influence lines in a non-contact manner. Ultimately, small and medium scale experimental tests were conducted and confirmed the applicability of the FRE method to beam structures. Results show that, even in presence of measurement noise (1%), the FRE framework predicts flexural rigidity with 95% accuracy.

Dedicated to...

My Beloved Parents,

My Dear Brother,

And My Lovely Wife.

TABLE OF CONTENTS

LIST OF TABLES	ix
LIST OF FIGURES	x
ACKNOWLEDGEMENTS	xiii
CHAPTER 1 INTRODUCTION	1
1.1 Background	1
1.2 Problem Statement and Methodology	2
CHAPTER 2 LITERATURE REVIEW	5
2.1 Structural Health Monitoring of Bridges	5
2.2 Influence Line-Based Structural Health Monitoring	7
2.3 Camera-Based Data Acquisition	9
2.4 Numerical Methods for Curve-Fitting Techniques	11
CHAPTER 3 DERIVATION OF THE FLEXURAL RIGIDITY ESTIMATION	13
3.1 Theoretical Framework	13
3.1.1 General Framework and Derivation for Flexural Rigidity Estimation	13
3.1.2 Alternate Derivation for Flexural Rigidity Estimation	16
3.2 Calculation of Moment $m(\xi)$	19
3.2.1 Statically Determinate Systems	19
3.2.2 Statically Indeterminate Systems	19

3.3	Analytical Procedures	23
3.3.1	Example 1 - Statically Determinate System.....	23
3.3.2	Example 2 - Statically Indeterminate System	24
3.4	Analytical Results and Discussion.....	26
3.4.1	Statically Determinate System	26
3.4.2	Statically Indeterminate System	27
CHAPTER 4 ANALYTICAL INVESTIGATION USING NOISY INFLUENCE LINE FOR FLEXURAL RIGIDITY ESTIMATION.....		31
4.1	Motivation.....	31
4.2	Curve-Fitting Using Parametric/Non-parametric Approximation Method.	31
4.2.1	Moving Window Method	32
4.2.2	Least-mean Square Error (LSQ) Method	34
4.2.3	Tikhonov Regularization Method.....	38
4.3	Performance Optimization of the Methods.....	42
4.4	FRE Using the Weighted Average of the Influence Lines	45
4.5	Analytical Modeling	46
4.6	Analytical Results and Discussion.....	48
CHAPTER 5 EXPERIMENTAL STUDIES		52
5.1	General Procedures	52
5.1.1	Camera-Based Data Acquisition	52
5.2	Determinate Beam	58
5.2.1	Procedure	58

5.2.2	Results and Discussion	60
5.3	Indeterminate Beam	62
5.3.1	Procedure	62
5.3.2	Verification of the Clamp Support	65
5.3.3	Results and Discussion	67
5.4	Scale-Model Bridge	71
5.4.1	Procedure	71
5.4.2	Verification Test	74
5.4.3	Results and Discussion	75
CHAPTER 6 SUMMARY, CONCLUSIONS, AND CONTRIBUTIONS		81
6.1	Summary	81
6.2	Specific Conclusions and Contributions	82
6.3	Future Work	82
APPENDIX A NOTATION LIST		83
REFERENCES		87

LIST OF TABLES

Table 3.1: Values of constant parameters.	24
Table 5.1: Bridge dimensions and material properties.	72

LIST OF FIGURES

Figure 3.1: Initial position and deflected shape of a beam structure under the effects of a unit load located at (a) ξ and (b) x_A	14
Figure 3.2: Deflected shape of the modified beam with a replaced hinge at the measurement point under the effects of a virtual displacement.....	18
Figure 3.3: Determinate beam.....	23
Figure 3.4: Considered statically-indeterminate beam.	24
Figure 3.5: Example 1 analysis results, (a) Recorded deflection influence line (DIL), (b) First derivative of the DIL, (c) Second derivative of the DIL, and (d) Beam flexural rigidity estimation (FRE).	27
Figure 3.6: Analysis results, (a) Recorded DIL, (b) First derivative of the DIL, (c) Second derivative of the DIL, (d) Diagram of moment $m(\xi)$, and (e) Beam flexural rigidity estimation (FRE).....	28
Figure 3.7: Analysis results, (a) Recorded RIL, (b) First derivative of the RIL, (c) Second derivative of the RIL, (d) Diagram of moment $m(\xi)$, and (e) Beam flexural rigidity estimation (FRE).....	30
Figure 4.1: (a) A simply-supported beam under the effects of a moving unit load, (b) Beam segmentation and locations of segments' centers (x_{si}), (c) Hypothetical illustration of a measured influence line and its theoretical path.	34

Figure 4.2 Considered Damaged Case Scenarios (a) Case 01 (b) Case 02.....	47
Figure 4.3: Damage Case 01, (a) NM = 40, (b) NM = 50, (c) NM = 100.	50
Figure 4.4: Damage Case 02, NM = 40.	50
Figure 5.1: Simplified pinhole imaging model.	54
Figure 5.2: Checkerboard target.	58
Figure 5.3: Experimental setup, (a) Front view, (b) Side view.	59
Figure 5.4: Cross-section reduction on the specimen.	59
Figure 5.5: Experimental results, (a) Measured RILs and fitted curves, (b) Results of flexural rigidity estimation (FRE).	61
Figure 5.6: Experimental setup.	63
Figure 5.7: Superposition of statically-determinate systems for calculation of moment curve for the main statically-indeterminate system.	64
Figure 5.8: Superposition of statically-determinate systems for calculation of moment at the clamped support for the main statically-indeterminate system.	65
Figure 5.9: Experimental setup for clamp support verification.	66
Figure 5.10: Tip deflection vs. load position for clamp verification.	67
Figure 5.11: Measured RILs, (a) at Point A, (b) at Point B.	68
Figure 5.12: FRE results for propped cantilever laboratory experiment.	69
Figure 5.13: FRE results for propped cantilever experiment, (a) NM = 5, (b) NM = 21.	70
Figure 5.14: Scale-model bridge with dimensions.	73
Figure 5.15 Considered damage case scenarios for scale-model experimental setup.	75
Figure 5.16: RIL for the intact bridge.	76

Figure 5.17: Damaged Case Scenario 01. Experimental Results Comparisons (a) MW, (b) LSQ, (c) TR. 78

Figure 5.18 Damaged Case Scenario 02. Experimental Results Comparisons (a) MW, (b) LSQ, (c) TR. 80

ACKNOWLEDGEMENTS

I would like to express my gratitude to my advisor, Brett Story, for his support, patience, and encouragement throughout my graduate studies. It is not often that one finds an advisor that always finds the time for listening to the little problems and roadblocks that unavoidably crop up in the course of performing research. His technical and editorial advice was essential to the completion of this dissertation. His supervision and advice has taught me innumerable lessons and insights in both my academic and personal life.

My thanks also go to the members of my committee, Dinesh Rajan, Khaled Abdelghany, Usama El Shamy, and Ali Heydari for providing many valuable comments that improved the presentation and contents of this dissertation.

My special thanks goes to Professor Rajan's research group members, Xinxiang Zhang, and Yamin li, for all their help during a joint research project where we studied the applicability of a machine-vision-based measurement setup.

I am also grateful to my colleague and friend Jase Sitton for helping me considerably with many parts of this research. Without his help, it was hardly possible for me to perform this level of accomplishment during my PhD era.

I am also thankful to the members of the SMU machine shop, Necdet Yildirimer and Kenneth Sangston for all their help during the construction of the experimental setup.

My parents, Nooshin and Hassan, and my brother, Yousof, receive my deepest gratitude and love. Despite the existent long distance between us, their continuous dedication and support in the many years of my studies, provided the foundation for this work.

Last, but not least, I would like to deeply thank my wife Sepide for her continued understanding and unfailing love during the past few years. You were always around at times I thought that it is impossible to continue, you helped me to keep things in perspective. Your support, encouragement, belief in me, and love was in the end what made this dissertation possible.

Financial support of this work in part received from SENSR, Structural Monitoring Solutions Company is also acknowledged.

CHAPTER 1

INTRODUCTION

1.1 Background

Society depends on critical infrastructure to support everyday activities. Civil Engineering infrastructure supports critical societal activities and provides: buildings for citizen dwellings, commercial enterprises, and governmental activities; roads, rails, and bridges for transportation; signs and signals for safety; and support structures for the delivery of necessary utility commodities such as power and water. Even as critical components of our civil infrastructure approach and exceed their design lives, demand on these structures continues to increase. This increased demand is driven by needs for increased efficiency in transportation, energy savings, etc. Uninterrupted service and operation in day to day societal activities cannot be achieved if civil infrastructure is structurally impaired and unable to effectively function.

The standard of practice and most trusted method for detection of impairments in our infrastructure is the human visual inspection. These visual inspections are expensive, slow, can be dangerous, and generally yield a qualitative assessment of the structure. If initial qualitative assessments warrant further evaluation, detailed inspections or analyses may be prescribed. These procedures, however, are often performed by specialists who did not perform the original assessment. A disconnect exists between quantitative data collected

with sensors and predominantly qualitative data collected by human inspectors. This disconnect provides opportunities for research that can aid infrastructure managers in detecting, classifying, and mitigating structural impairments. The focus of research efforts on monitoring, evaluating, maintaining, and addressing challenges associated with aging infrastructure have resulted in the development of the field of structural health monitoring (SHM). Data collected from SHM can complement other information in the search for a better understanding of the mechanisms of decaying structures and prevent these structures from premature and unexpected failure (ASCE, 2017; Das, Saha, & Patro, 2016; Doebling, Farrar, & Prime, 1997; Fan & Qiao, 2011; Rytter, 1993; Seo, Hu, & Lee, 2016; Sohn, Farrar, Hemez, & Czarnecki, 2002; Story, 2012; Worden & Dulieu-Barton, 2004).

Bridges represent one critical component of national infrastructure and are aging, deteriorating, and exhausting their capacity to meet the operational demands over time in typical service conditions (ASCE, 2017). The U.S. has 614,387 bridges, almost four in 10 of which are 50 years or older. In 2017, the America's bridges were graded as C+ by ASCE Infrastructure Report Card. This report states that 56,007 (9.1%) of the nation's bridges were structurally deficient in 2016. The most recent estimate puts the nation's backlog of bridge rehabilitation needs at \$123 billion (ASCE, 2017).

1.2 Problem Statement and Methodology

The goal of this dissertation research is to develop a structural impairment detection (SID) system that utilizes static deformation influence lines (IL) to estimate the flexural rigidity of beam structures. The requirements of such a flexural rigidity estimation (FRE) include: foundation in mechanical theory; sensitivity to structural impairment (considering

specific modalities of measurement); and consistency, efficacy, and efficiency of the technique in practice (Story & Fry, 2014b; Turer, 2000; R. Zaurin & Catbas, 2010; Ricardo Zaurin & Catbas, 2011). The logical, mechanical motivation for implementing an IL-based flexural rigidity estimation (FRE) is as follows:

1. Structural impairments in beam structures may manifest as changes in flexural rigidity,
2. Changes in flexural rigidity affect the deformation (i.e. deflection and rotation) of beam structures,
3. Changes in deformation may be assessed by extracting deformation influence lines from beam structures using both contact and non-contact methods.

This dissertation describes the theoretical framework of the relationship between the second derivative of deformation influence line and flexural rigidity in an Euler-Bernoulli beam. This framework is used to calculate the FRE along a beam by quantifying the loading condition and measuring displacement or rotation at one or more locations. In field applications of this method, the rotation or deflection influence line of a specific point is recorded and the resulting IL is constructed. In practice, measurement errors are unavoidable and the challenge of constructing a useful second derivative of noisy data must be addressed. The FRE framework is a theoretically robust damage index; however, the sensitivity of the method to unavoidable noise in deformation measurements necessitates an analysis method robust against such measurement noise.

The following methodology is employed in this dissertation:

1. Establish the theoretical, mechanical relationship between the deformation IL (specifically, the second spatial derivative of the deformation IL) and the flexural rigidity,
2. Characterize the effect of measurement noise on the sensitivity and consistency of the method, and
3. Develop and demonstrate a practical data acquisition system for estimating deformation ILs.

Specifically, a computer-vision technique and multiple numerical algorithms are integrated with the mechanical theory to form the FRE framework. Ultimately, analytical investigations and controlled experiments at multiple scales are presented.

CHAPTER 2

LITERATURE REVIEW

2.1 Structural Health Monitoring of Bridges

Bridges deteriorate structurally over time in typical service conditions. Detecting, classifying, and mitigating structural impairments are significant challenges for structural engineers, inspectors, and owners. The field of structural health monitoring (SHM) has developed to address these challenges associated with aging infrastructure (ASCE, 2017; Das et al., 2016; Doebling et al., 1997; Fan & Qiao, 2011; Rytter, 1993; Seo et al., 2016; Sohn et al., 2002; Story, 2012; Worden & Duijveland, 2004). Rytter outlines criteria for classification of SHM algorithms into four levels based on their output information (Rytter, 1993). At the simplest level (level 1), the SHM algorithm should provide a general indication of damage, while in levels 2–4 additional information regarding damage location, severity, and remaining service life of the structure will be provided, respectively. Algorithms utilizing appropriate structural health indices may increase the SHM classification level and aid engineers in adequately rating structural condition. Appropriate indices include the following essential features (Story & Fry, 2014c; Turer, 2000; Zaurin & Catbas, 2010; Zaurin & Catbas, 2011):

1. Foundation in mechanical theory
2. Sensitivity to impairment

3. Consistency in the evaluation technique
4. Efficacy and efficiency of the technique in practice

Damage indices are typically defined based on dynamic responses (Das et al., 2016; Doebling et al., 1997; Fan & Qiao, 2011, Bakeer, 2016; Dzunic, Chen, Mobahi, Büyüköztürk, & Fisher, 2017; Yang, Radzienski, Kudela, & Ostachowicz, 2017a, 2017b; Zhang, Li, Hao, & Ma, 2017), or static responses (Story & Fry, 2014c, 2014a; Turer, 2000; Turer, Levi, & Aktan, 1998; Zaurin & Catbas, 2010; Ricardo Zaurin & Catbas, 2011; Ricardo Zaurin, Khuc, & Catbas, 2015; Zeinali & Story, 2017). Both static and dynamic methods have strengths and shortcomings. Sensors that measure dynamic responses (e.g. accelerometers) are typically easier to install and implement while sensors that measure static responses (e.g. strain gages, LVDTs) may require significant installation effort. Damage identification methods that are based on dynamic responses, are classified into four major categories: natural frequency-based methods, mode shape-based methods, curvature mode shape-based methods, and methods using both mode shapes and frequencies. Most of the mode shape based methods and curvature mode shape-based methods only focus on damage localization. High level of dependencies of these methods on optimization algorithms and signal processing techniques are a common drawback in all of these methods (Fan & Qiao, 2011). Static deformation measurements may be less affected by noise resulting from transient, incidental vibration or environmental changes and, thus, may relate known load and unknown condition more clearly than noisier dynamic signals (Chang, Flatau, & Liu, 2003; Cross, Koo, Brownjohn, & Worden, 2013; Sun, Nagayama, & Fujino, 2016).

Many damage scenarios reduce a structural system's stiffness; these stiffness degradations affect system deformations and lead to structural impairment (Story & Fry, 2014a; Zeinali & Story, 2016). Significant advancements in state of the art of deformation estimations (e.g., camera-based systems) and their increasing applications present opportunities for monitoring frameworks that utilize deformation data streams (Feng & Feng, 2017; Oh, Hwang, Kim, Cho, & Park, 2015; Sładek et al., 2013). This dissertation presents an index and technique for locating and quantifying reductions in flexural rigidity along a beam structure by analyzing deformation influence lines at a single location on the beam.

2.2 Influence Line-Based Structural Health Monitoring

An influence line function represents the magnitude of a desired response (e.g., strain, shear, moment, deflection, rotation, etc.) at a fixed point on a structural system that is caused by a static load pattern placed anywhere on the structure. If the load pattern is limited to a single unit load, the influence line is called a Unit Influence Line (UIL). The UIL technique has been implemented widely in bridge engineering design and load rating.

A system's static response influence lines are comprehensive evaluation indices that contain many of the previously outlined features that are rich in diagnostic content (Catbas, Zaurin, Susoy, & Gul, 2007; Chen, Zhu, Xu, Li, & Cai, 2015; Turer, 2000; Turer et al., 1998; Zaurin & Catbas, 2010; Zaurin & Catbas, 2011). Several studies utilizing an influence line approach for bridge evaluation and monitoring are outlined in the literature. Many of these studies utilize the internal responses, such as strain (Catbas, Zaurin, Gul, & Gokce, 2012; Catbas et al., 2007; Zaurin & Catbas, 2010; Zaurin & Catbas, 2011; Zaurin et al., 2015) or stress influence lines (Bernal, 2014; Chen et al., 2015). Others use global

deformation influence lines (Catbas et al., 1998; Turer, 2000; Turer et al., 1998). Changes in flexural rigidity anywhere along a span will manifest in the global deformation influence lines at any other point on the beam, regardless of the determinacy of the system.

The preliminary efforts of employing deformation influence lines as a bridge condition index gathered measurements from diagnostic crawl-speed tests and derived the unit load influence line using numerical decomposition (Catbas et al., 1998; Turer, 2000; Turer et al., 1998). Turer utilized two methods, the energy method and the direct stiffness method, to show that a conceptual relation between flexibility and deformation influence coefficients exists (Turer, 2000). In the energy method, an approximation-of-energy-based equation for computation of the deflected shape of a beam with variable cross section stiffness over a uniformly distributed number of segments is utilized to drive the relation. In the direct stiffness method, the matrix-based relation between element stiffness matrices, applied loads, and the displacement of the system are utilized (Turer, 2000). The latter method is conceptually similar to the model updating approach that is studied and recommended in the literature (Bernal, 2014). Due to poor conditioning of the problem in the applications on full-scale structures, reaching a successful solution using finite element model updating is difficult (Bernal, 2014).

Over the past decade, various studies have proposed a method to locate damage by analyzing the absolute differences between the curvatures of the deflection influence lines for intact and damaged beam structures (Stimac & Grandic, 2014; Stimac, Grandic, & Bjelnovic, 2011; Ivana Stimac, Mihanovic, & Kozar, 2006; Wang & Liu, 2014). Zaurin et al. (2016) and Chen et al. (2015) explored a group of damage localization indices based on noisy stress and deflection influence lines for long-span and mid-span bridges,

respectively. The performances of the proposed methods were evaluated through numerical and experimental case studies (Chen et al., 2015; Zaurin et al., 2015). The recent work of Chen et. al. (2015) introduces a matrix decomposition method for damage quantification of beam structures using deflection influence lines. In this study, the eigen-parameter decomposition of a stiffness matrix was used to reconstruct a deflection influence line matrix, and then, the relationship between UIL and damage extent is explicitly demonstrated. While the proposed solution by Chen et. al. is mathematically able to give an effect solution for localization and quantification of the damages, the method requires high resolution sensors and need for placement of multiple sensors along the structure for UIL measurement. Also, a high rate of false alarms was observed in the presence of noise.

2.3 Camera-Based Data Acquisition

Monitoring the global movements of a structural system provides significant insight into the structural health condition of the system (Ye, Dong, & Liu, 2016; Zeinali & Story, 2017, 2018). Accurate measurement of the global displacements of structures in field conditions presents challenges, including the cost and the need for large arrays of instrumentation (Feng & Feng, 2017; Ribeiro, Calçada, Ferreira, & Martins, 2014; Robson, MacDonald, Kyle, & Shortis, 2016; Santini-Bell et al., 2010). The application of an accurate non-contact computer-vision based movement measurement (CVMM) system addresses these challenges and provides a solution for the accurate measurement of structural movements. CVMM systems facilitate robust, real-time automated structural health monitoring (SHM). The application of high-resolution cameras and powerful new

computer-vision algorithms can achieve an accurate, safe, cost-effective, real-time, and reliable movement measurement system. A non-contact CVMM system can decrease operating risks and human errors.

Computer-vision based movement measurement systems have seen widespread application in infrastructure monitoring in recent years. Generally, CVMM systems are classified into target-less (Feng & Feng, 2016, 2017; Feng, Feng, Ozer, & Fukuda, 2015) or target-based methods (Chang & Xiao, 2010; Choi, Cheung, Kim, & Ahn, 2011; Fukuda, Feng, & Shinozuka, 2010; Oh et al., 2015). In target-less CVMM systems, the movement of distinct features on the monitored object, such as the corners or edges of the structure, are tracked. Target-less CVMM systems have more uncertainty during system installation as these systems are sensitive to the illumination of the environment, the quality of the camera setup (e.g. lens distortion), or uncertainty in the direction of the structure's movement (Chen et al., 2017; Feng, Scarangelo, Feng, & Ye, 2017; Ye et al., 2016). A critical assumption in these methods is that the illumination of the environment remains unchanged during the measurement, otherwise false perceived motion due to changes in illumination would also be captured (Chen et al., 2017).

In target-based CVMM systems, distinct targets, such as black-and-white checkerboards, are mounted on the monitored structure. Computer-vision techniques, including camera calibration methods, are then implemented to automatically detect and track the movement of the targets in the acquired images (Heikkila & Silven, 1997; Janne Heikkila, 2000; Zhang, 2000). The application of target-based CVMM systems with a robust camera calibration technique may give a more reliable and accurate movement measurement system than the application of target-less CVMM systems (Busca, Cigada,

Mazzoleni, & Zappa, 2014; Ferrer, Mas, García-Santos, & Luzi, 2016; Shan, Wang, Huo, Yuan, & Xue, 2016).

Monocular camera systems, which have recently been used for measuring the movement of structural systems, estimate the structural displacements parallel to the image plane (Kohut, Holak, & Martowicz, 2012; Robson et al., 2016; Sładek et al., 2013). To measure the movements perpendicular to the image plane, stereo-vision methods (Chang & Ji, 2007; Shan, Zheng, & Ou, 2015) or depth-camera methods (Franco, Mayag, Marulanda, & Thomson, 2017) or Kinect have been used, however these methods are expensive and require time-consuming image synchronization (Chen, Wu, Tseng, Chen, & Lai, 2015; Hu et al., 2012).

2.4 Numerical Methods for Curve-Fitting Techniques

The process of constructing a mathematical formula that has the best fit to the available data, is called curve fitting. The fitted curve could have a predefined shape (parametric fitting), or its shape is defined according to the shape of the available data (non-parametric fitting). In this research, both approaches are utilized to construct the fitting function. In Moving-window method, the shape of the second derivative at each point is constructed based on the neighbor available data.

As an application of a parametric function fitting, the least mean square (LSQ) method is presented in this research. In this method, a predefined cubic spline curve with variable number of segment that is constrained to a specific boundary conditions, is selected and fitted to the available data. No matter what type of curve fitting is utilized, have low number of measurement with respect to the available unknown parameters in the model

will generate an ill-posed or over-fitted curve. To overcome this challenge, a common and robust regularization method called Tikhonov Regularization method is utilized.

The fundamental idea of the regularization method, used to solve the approximation problem in this study, is to constrain the solution on the smoothness of the fitted curve. Many direct regularization methods exist: Tikhonov Regularization (TR), Truncated Singular Value Decomposition (TSVD), or Methods of Lines (ML). Among these methods, TR is one of the most common methods and is selected for use in this study (Hardle, 1991; Simonoff, 1996; Tikhonov, Goncharsky, Stempanov, & Yagola, 1995).

Theoretically, the TR method is able to solve ill-posed parametric curve fitting problems; however, the regularized results achieved by this method can be improved. To increase the performance of the regularization method, an Iterative Multi-parameter Tikhonov Regularization method is presented and applied to an influence line based impairment detection problem, (i.e. FRE estimation).

CHAPTER 3

DERIVATION OF THE FLEXURAL RIGIDITY ESTIMATION

3.1 Theoretical Framework

3.1.1 General Framework and Derivation for Flexural Rigidity Estimation

This dissertation presents a theoretical framework, utilizing static deformation influence lines to estimate the flexural rigidity of Euler-Bernoulli beams. In the proposed flexural rigidity estimate (FRE) formula, the relationship between the second derivative of deformation influence line and the flexural rigidity for both statically determinate and indeterminate beam structures is:

$$EI(x) = \frac{m(x)}{u''_{x_A}(x)} \quad (3.1)$$

In Eq. (3.1), $u''_{x_A}(x)$ is the second derivative of rotation or deflection influence line (RIL or DIL, respectively) at a specific point (x_A), $EI(x)$ is the flexural rigidity of the cross-section at location x , and $m(x)$ is the resultant internal moment caused by a unit load (in case of using DIL) or a unit moment (in case of using RIL) applied at the location of point x_A .

A straight beam with linear elastic material and two-dimensional linear geometric behavior is illustrated in Figure 3.1a. A unit force is applied on this beam at distance ξ from the left support location. The vertical deflection, $y(x, \xi)$, (dashed lines in Figure

3.1a) is a function of the location of the unit load, ξ , and varies with the position along the beam. The first argument in the function $y(x, \xi)$ represents the monitoring location along the beam. The second argument is the location of the unit load. If the first argument varies and the second is fixed, then y is a deflection function when the unit load is fixed; if the opposite is true, then y is a DIL of the fixed first argument.

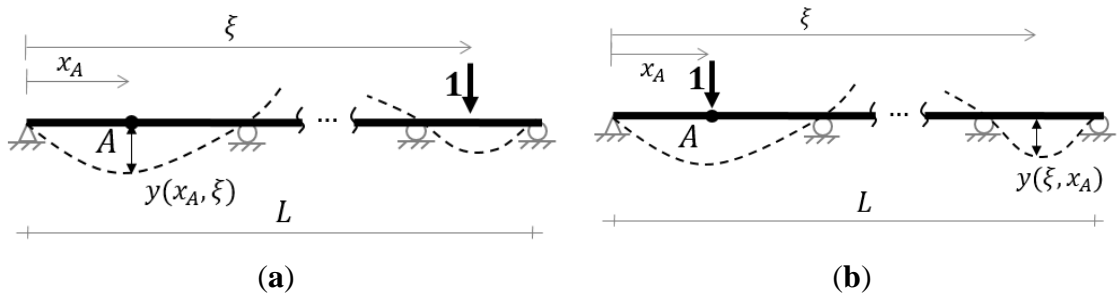


Figure 3.1: Initial position and deflected shape of a beam structure under the effects of a unit load located at (a) ξ and (b) x_A .

The vertical deflection influence line (DIL) of an arbitrary point A located at distance x_A from the left support, $y(x_A, \xi)$, is defined as the deflection of the beam at point A as a unit load located at ξ traverses the span, i.e., $(0 < \xi < L)$.

According to Maxwell's theorem of reciprocal displacement, the deflection at point A due to a unit load acting at distance ξ (i.e., $y(x_A, \xi)$) is equal to the beam deflection at distance ξ when the unit load is acting at point A (i.e., $y(\xi, x_A)$). So, using Maxwell's theorem gives:

$$y(x_A, \xi) = y(\xi, x_A) \quad (3.2)$$

If ξ varies from 0 to L , the left side of Eq. (3.2) is the DIL of point A , and the right side of Eq. (3.2) represents the beam's deflected shape when a unit load is applied at point A . This is illustrated in Figure 3.1b.

Assuming that both sides of Eq. (3.2) are twice differentiable, differentiating both sides of Eq. (3.2) twice with respect to ξ yields:

$$\frac{\partial^2 y(x_A, \xi)}{\partial \xi^2} = \frac{\partial^2 y(\xi, x_A)}{\partial \xi^2} \quad (3.3)$$

The left side of Eq. (3.2) may be acquired practically by collecting deflection data at point A as a unit load traverses the structure and differentiating twice.

The right side of Eq. (3.2) represents the deflected shape of the beam when a unit load is located at x_A ; therefore, the right side of Eq. (3.3) is the beam curvature when a unit load is applied at distance x_A . If Euler-Bernoulli behavior is considered, then the right side of Eq. (3.3) can be related to internal moment and flexural rigidity:

$$\frac{\partial^2 y(x_A, \xi)}{\partial \xi^2} = \frac{\partial^2 y(\xi, x_A)}{\partial \xi^2} = \frac{m(\xi)}{EI(\xi)} \quad (3.4)$$

In Eq. (3.4), $EI(\xi)$ is the current beam flexural rigidity at ξ and may be a variable function along the beam. Moreover, the moment $m(\xi)$ is the internal moment when a unit load is acting at point A .

By using Maxwell's reciprocal theorem and the same procedure, it can be shown that Eq. (3.4) is also valid for the rotation influence line (RIL). In the case of using the RIL instead of the DIL (i.e., $\theta(x_A, \xi)$ instead of $y(x_A, \xi)$), the moment $m(\xi)$ in Eq. (3.4) equals the internal moment when a unit moment is acting at the point A .

For simplification and generalization, the term $y(x_A, \xi)$ (or $\theta(x_A, \xi)$) is replaced with $u_A(\xi)$. Eq. (3.4) becomes:

$$u_A''(\xi) = \frac{m(\xi)}{EI(\xi)} \quad (3.5)$$

Practically, $EI(\xi)$ will never be equal to zero in Eq. (3.5). So, in regions that $m(\xi)$ is zero,

$u_A''(\xi)$ becomes zero and in regions that $m(\xi)$ is not equal to zero, Eq. (3.5) yields Eq. (3.1). Eq. (3.1) is the Flexural Rigidity Estimate (FRE), which provides $EI(\xi)$, the beam's flexural rigidity at location ξ as a function of a known internal moment $m(\xi)$ and the second derivative of a measured *DIL* or *RIL*, $u_A''(\xi)$.

By comparing the nominal flexural rigidity (EI_0) with the FRE calculated from Eq. (3.1), the location and quantity of the impairment to the flexural rigidity can be estimated. In practice, the influence line is extracted by solving an inverse problem. First, the desired response (e.g., vertical deflection or rotation) of a specific location is recorded. Then, by synchronizing the recorded measurement with the location of moving loads (e.g., vehicular loads) and solving an inverse problem, the influence line, $u_A(\xi)$, of a unit load can be extracted (F. Necati Catbas et al., 2012; F Necati Catbas et al., 2007; Turer, 2000; Turer et al., 1998; R. Zaurin & Catbas, 2010; Ricardo Zaurin & Catbas, 2011; Ricardo Zaurin et al., 2015).

The second derivative of $u_A(\xi)$ can be estimated numerically. The moment $m(\xi)$ in Eq. (3.1) must be calculated or estimated.

3.1.2 Alternate Derivation for Flexural Rigidity Estimation

The deflection of point *A* in Figure 3.1 as a function of a traversing unit load, $u_A(\xi)$, can be calculated using the flexural equation for virtual work.

In the case of linear geometry, elastic material behavior, and negligible shear deformations, the small flexural deflection $u_A(\xi)$, under the effects of a unit load at distance ξ is expressed as:

$$u_A(\xi) = \int_0^L \frac{M(x, \xi) \cdot m(x)}{EI(x)} dx \quad (3.6)$$

In Eq. (3.6), the moment $M(x, \xi)$ is the beam internal moment caused by an externally applied load (i.e., the moving unit load) and $m(x)$ is the internal moment caused by a virtual unit load applied at point A . The moment $m(x)$ is a function of location x_A , but independent of variable ξ .

The moment $M(x, \xi)$ in Eq. (3.6) is the only parameter on the right side that is a function of ξ . Both $m(x)$ and $EI(x)$ remain constant as a unit load traverses the beam. Hence, the first and second derivatives of $u_A(\xi)$ with respect to ξ are equal to Eqs. (3.7) and (3.7), respectively.

$$\frac{du_A}{d\xi} = u'_A(\xi) = \int_0^L \frac{\frac{\partial M(x, \xi)}{\partial \xi} \cdot m(x)}{EI(x)} dx \quad (3.7)$$

$$\frac{d^2 u_A}{d\xi^2} = u''_A(\xi) = \int_0^L \frac{\frac{\partial^2 M(x, \xi)}{\partial \xi^2} \cdot m(x)}{EI(x)} dx \quad (3.8)$$

The moment $M(x, \xi)$ in Eq. (3.6) is the internal moment influence line at point x . According to the Muller-Breslau principle, the influence line for this internal moment is the scaled deflected shape of a beam with released moment resistance that is subject to a virtual displacement at a frictionless hinge. This modified beam with an internal hinge is depicted in Figure 3.2. In other words, the moment $M(x, \xi)$ is equal to:

$$M(x, \xi) = \frac{1}{\alpha_x} y_{M.B.}(\xi) \quad (3.9)$$

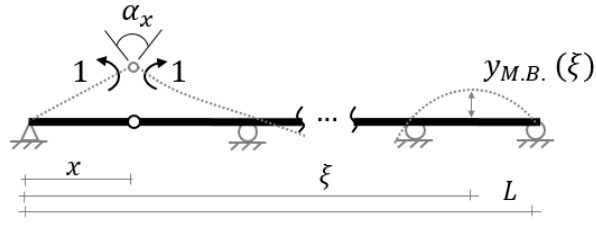


Figure 3.2: Deflected shape of the modified beam with a replaced hinge at the measurement point under the effects of a virtual displacement.

In Eq. (3.9), $y_{M.B.}(\xi)$ and α_x are the deflection curve and angular displacement at x of the modified beam under the effects of a virtual displacement, as illustrated in Figure 3.2.

The second derivative of moment M with respect to ξ is equal to:

$$\frac{\partial^2 M(x, \xi)}{\partial \xi^2} = \frac{1}{\alpha_x} \frac{d^2 y_{M.B.}}{d\xi^2} \quad (3.10)$$

The right side of Eq. (3.10) is related to the curvature of the modified beam that is subject to a small virtual displacement, as shown in Figure 3.2. For the case of a statically determinate beam, the moment influence line is linear, so the curvature of the deflected shape of the modified beam must be zero except for at the location of the hinge, where the curvature is infinite. Hence, the right side of Eq. (3.10) is equal to:

$$\frac{1}{\alpha_x} \frac{d^2 y_{M.B.}}{d\xi^2} = \begin{cases} 0 & \xi \neq x \\ \infty & \xi = x \end{cases} \quad (3.11)$$

The right side of Eq. (3.11) is the Dirac delta function centered at $\xi = x$. Substituting Eqs. (3.10) and (3.11) into Eq. (3.8) gives:

$$u_A''(\xi) = \int_0^L \frac{\delta(x - \xi) \cdot m(x)}{EI(x)} dx \quad (3.12)$$

According to the properties of the Dirac delta function, when $0 < \xi < L$, Eq. (3.12) yields:

$$u_A''(\xi) = \frac{m(\xi)}{EI(\xi)} \quad (3.13)$$

This is the same as Eq. (3.5). Superposition is used when applying the framework to statically indeterminate structures as shown in the following section.

3.2 Calculation of Moment $m(\xi)$

The moment $m(\xi)$ is independent of a statically determinate system's flexural stiffness; conversely, the moment $m(\xi)$ is dependent upon a system's flexural stiffness if the system is statically indeterminate. The methods for calculating and estimating the moment $m(\xi)$ outlined below.

3.2.1 *Statically Determinate Systems*

In a statically determinate system, $m(\xi)$ is not a function of beam flexural stiffness, but is a function of the location (x_A) and the type of recorded deformation. Hence, no additional information is required to calculate the $m(\xi)$ diagram.

In the case of using a DIL:

$$m(\xi) = \begin{cases} \frac{\xi(L - x_A)}{L} & \xi \leq x_A \\ \frac{x_A(L - \xi)}{L} & \xi > x_A \end{cases} \quad (3.14)$$

In the case of using a RIL:

$$m(\xi) = \begin{cases} \frac{\xi}{L} & \xi \leq x_A \\ \frac{\xi}{L} - 1 & \xi > x_A \end{cases} \quad (3.15)$$

3.2.2 *Statically Indeterminate Systems*

In a statically indeterminate system (e.g., a continuous multi-span beam), the moment $m(\xi)$ is a function of the system's flexural stiffness. Hence, calculation of the moment

$m(\xi)$ requires additional information. Two techniques are described to calculate and estimate the moment $m(\xi)$ for both DIL and RIL

3.2.2.1 Deflection Influence Line (DIL)

In the case of using a DIL, the moment $m(\xi)$ will be the diagram of the moment that is created by a unit load that is applied at distance x_A . In a linear system, the response of a statically indeterminate or continuous beam with a degree of indeterminacy (DOI , i.e., the number of interior vertical support reactions) can be calculated by the superposition of $DOI + 1$ number of statically determinate systems (i.e., simply supported beams). For this purpose, each vertical support (support i) is replaced by a vertical reaction R_i . The moment $m(\xi)$ of the continuous beam is calculated by the superposition of moment in these $DOI + 1$ statically determinate simply supported beams:

$$m(\xi) = m_{UL}(\xi) + \sum_{i=1}^{DOI} R_i m_i(\xi) \quad (3.16)$$

In Eq. (3.16), $m_{UL}(\xi)$ is the moment that is caused by a unit load applied at a distance x_0 on a simply supported beam. Moment $m_i(\xi)$ is the moment that is caused by a unit load that is applied on the simply supported beam at location of the interior support i . If x_i serves as the location of interior support, i , the equations for m_{UL} and m_i are as follows:

$$m_{UL}(\xi) = \begin{cases} \frac{\xi(L - x_A)}{L} & \xi \leq x_A \\ \frac{x_A(L - \xi)}{L} & \xi > x_A \end{cases} \quad (3.17)$$

$$m_i(\xi) = \begin{cases} \frac{\xi(L - x_i)}{L} & \xi \leq x_i \\ \frac{x_i(L - \xi)}{L} & \xi > x_i \end{cases} \quad (3.18)$$

Moreover, in Eq. (3.16), reaction R_i is the reaction of interior support i when a unit load is applied on a continuous beam at distance $\xi = x_A$. These reactions are unknown and additional information about the flexural rigidity at the interior supports is required. For example, this additional information could be obtained by estimating the strain at each support location using strain gages.

By having knowledge about the status of the flexural rigidity on interior support locations, the internal moment at each support location can be calculated by converting the recorded strains.

Thus, when the moving unit load is located at a distance $\xi = x_A$, the moment at each support can be estimated from the measured strain. These moments constitute the moment $m(\xi)$ at each support location (i.e., $m(x_1), m(x_2), \dots, m(x_{DOI})$). So,

$$\begin{bmatrix} m(x_1) \\ \vdots \\ m(x_{DOI}) \end{bmatrix}_{DOI \times 1} = \begin{bmatrix} m_{UL}(x_1) \\ \vdots \\ m_{UL}(x_{DOI}) \end{bmatrix}_{DOI \times 1} + \begin{bmatrix} m_1(x_1) & \dots & m_{DOI}(x_1) \\ \vdots & \ddots & \vdots \\ m_1(x_{DOI}) & \dots & m_{DOI}(x_{DOI}) \end{bmatrix}_{DOI \times DOI} \times \begin{bmatrix} R_1 \\ \vdots \\ R_{DOI} \end{bmatrix}_{DOI \times 1} \quad (3.19)$$

Or, in matrix format:

$$\tilde{\mathbf{m}} = \tilde{\mathbf{m}}_{UL} + [\tilde{\mathbf{m}}_1 \quad \tilde{\mathbf{m}}_2 \quad \dots \quad \tilde{\mathbf{m}}_{DOI}] \times \tilde{\mathbf{R}}_i \quad (3.20)$$

As can be seen in Eq. (3.20), the measured moments give DOI number of equations with DOI number of unknowns (R_i). By solving Eq. (3.20), the unknowns R_i can be solved as:

$$\tilde{\mathbf{R}}_i = [\tilde{\mathbf{m}}_1 \quad \tilde{\mathbf{m}}_2 \quad \dots \quad \tilde{\mathbf{m}}_{DOI}]^{-1} \times (\tilde{\mathbf{m}} - \tilde{\mathbf{m}}_{UL}) \quad (3.21)$$

Therefore, when a DIL is measured, the moment $m(\xi)$ of the continuous beam can be constructed by substituting the resultant R_i from Eq. (3.21) in Eq. (3.16).

3.2.2.2 Rotation Influence Line (RIL)

In the case of measuring the RIL, the moment $m(\xi)$ is the moment that is caused by a concentrated unit moment at measurement location (x_A). The influence line is constructed using a unit point load; the technique proposed for using a deflection influence line is not applicable here, and the measured moments (i.e., $m(x_1), m(x_2), \dots, m(x_{DOI})$) must be preprocessed.

The first derivative of the deflection influence line can be explained using Eq. (3.22):

$$\frac{du}{d\xi} = \lim_{\Delta\xi \rightarrow 0} \frac{u(\xi + \Delta\xi) - u(\xi)}{\Delta\xi} \quad (3.22)$$

The right side of Eq. (3.22) can be expanded to:

$$u' = \lim_{\Delta\xi \rightarrow 0} \frac{u(\xi + \Delta\xi)}{\Delta\xi} - \frac{u(\xi)}{\Delta\xi} \quad (3.23)$$

According to the definition of the deflection influence line, $u(\xi)$ is the beam deformation at a location x_0 when a unit load is applied at a distance ξ . So, in Eq. (3.22), the terms $\frac{u(\xi+\Delta\xi)}{\Delta\xi}$ and $\frac{u(\xi)}{\Delta\xi}$ are the beam deformations at location x_0 when a moving load with intensity equal to $\frac{1}{\Delta\xi}$ is applied at distances $\xi + \Delta\xi$ and ξ , respectively. By using the principle of superposition, u' in Eq. (3.22) is the beam deformation under the effects of two concentrated loads that are applied in opposite directions. These concentrated loads can be replaced by a couple with intensity equal to:

$$M = \frac{1}{\Delta\xi} \times \Delta\xi = 1 \quad (3.24)$$

As $\Delta\xi$ approaches zero, the location of this couple approaches ξ . This means that $u'(\xi)$ is the beam deformation at location x_0 that is caused by a positive unit moment applied at location ξ . The first derivative of the deformation influence line under the effects

of a moving unit load can be interpreted as the deformation influence line under the effects of a moving unit moment.

In a similar manner, the first derivative of the recorded moment measurement at each interior support location can be assumed as interior support moment under the effects of moving unit moment. By taking the first derivative of the recorded moment at each interior support location, the moment $m(\xi)$ at each support location (i.e., $m(x_1), m(x_2), \dots, m(x_{DOI})$) is determined. In this section, $m_i(\xi)$ has the same definition used in Eq. (3.18). By gathering this information, Eq. (3.5) still can be utilized to calculate the diagram of moment $m(\xi)$.

3.3 Analytical Procedures

3.3.1 Example 1 - Statically Determinate System

Figure 3.3 depicts a simply supported beam with a reduction in flexural rigidity from EI_0 (nominal rigidity) to βEI_0 ($0 < \beta < 1$) between locations L_1 and L_2 . The deflection influence line of the beam at location x_0 is available from recorded deflection data.

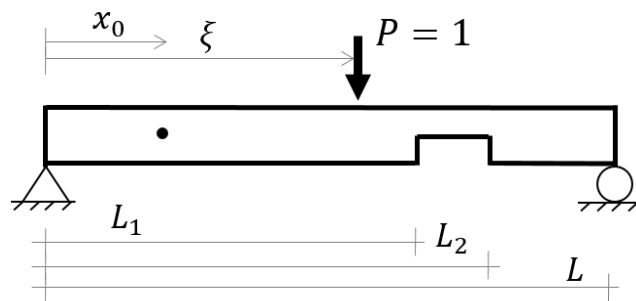


Figure 3.3: Determinate beam.

Using the arbitrary values that are listed in Table 3.1, a finite element (FE) model was created to solve the defined problem. The OpenSees software was utilized for generation

of the FE model (Mazzoni, McKenna, Scott, & Fenves, 2006). Elastic beam column elements (*ElasticBeamColumn*) were used to construct the model. This is a linear element that considers an Euler-Bernoulli model for each element. Each element has a node at each end, and each node has three global degrees of freedom: two translations and one rotation. At one support, all translation is fixed; on the other end, only vertical translation is fixed. By using the FE model, the DIL was calculated. In this solution, the beam was divided into 1500 elements, with flexural stiffness and two degrees of freedom at each node.

Table 3.1: Values of constant parameters.

Parameter	Value	Unit
EI_0	10	Force \times Length ²
β	0.6	-
L	10	Length
x_0	2	Length
L_1	6	Length
L_2	7	Length

3.3.2 Example 2 - Statically Indeterminate System

Figure 3.4 illustrates a statically indeterminate system similar to the one in Example 1 but with an additional interior support located at $x_1 = 4$.

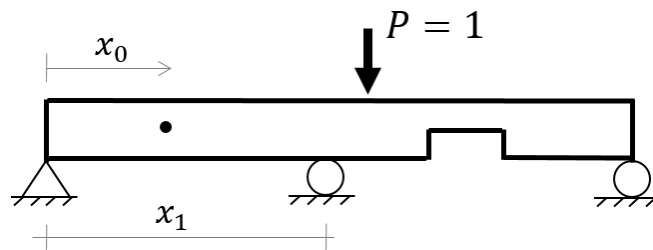


Figure 3.4: Considered statically-indeterminate beam.

3.3.2.1 Using Deflection Influence Line (DIL)

In this section, the DIL is implemented to solve the damage detection problem in Example 2. The moment, $m(\xi)$, is a function of the system's flexural rigidity in

indeterminate systems, and its calculation requires additional information. To obtain this additional information, a strain gage is attached to the cross-section at the interior support location. If the status of the flexural rigidity at this cross-section is already known, the measured strains at this cross-section can be converted to internal moment at this location.

The moment is calculated from strain that occurs when the moving unit load is located at distance $\xi = x_A$. This moment is substituted into Eq. (3.21). The resultant R_1 is then substituted into Eq. (3.16) and the general function of moment $m(\xi)$ in this two-span continuous beam is constructed.

3.3.2.2 Using Rotation Influence Line (RIL)

If the beam rotation influence line at an interior support is used, then the $m(\xi)$ diagram will have a discontinuity at the location of the interior support. The function $m(\xi)$ is not defined at this point, and the location of this jump is the only point at which the corresponding flexural rigidity cannot be calculated using Eq. (3.1). However, according to the procedure defined in Section 3.2.2, it is required that the status of beam cross-section on interior support locations be investigated in order to implement the proposed method in a statically-indeterminate system; therefore, the only cross-section that could not be monitored by using the RIL is already diagnosed.

In other words, by using the RIL, the theoretical solution for the flexural rigidity of all cross-sections can be accurately assessed. If the central difference method is used for calculating the second derivative, then using the beam RIL at an interior support location, rather than the DIL, is recommended.

3.4 Analytical Results and Discussion

3.4.1 *Statically Determinate System*

The resultant DIL and its first and second derivatives are plotted in Figure 3.5a–c, respectively. In practice, the resultant DIL is a series of points. Hence, to get the first and second derivatives, numerical methods should be utilized. To get the second derivative in this example, the second order central difference method (CDM) with three points is implemented. Moreover, the piecewise equation of moment m , the resultant moment that is caused by a unit point load applied at distance x_0 on a simply supported beam, is equal to Eq. (3.14).

By substituting the calculated second derivative and Eq. (3.14) into Eq. (3.1), the beam's flexural rigidity can be calculated. The resultant flexural rigidity is illustrated in Figure 3.5d.

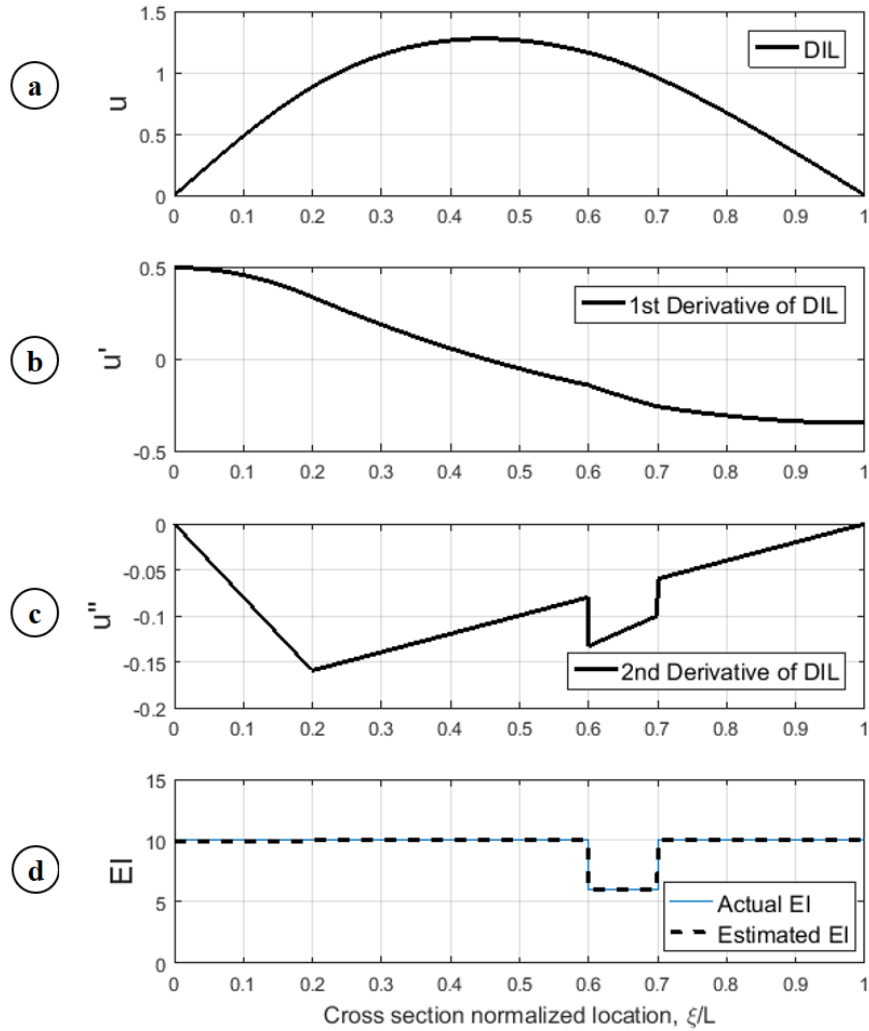


Figure 3.5: Example 1 analysis results, (a) Recorded deflection influence line (DIL), (b) First derivative of the DIL, (c) Second derivative of the DIL, and (d) Beam flexural rigidity estimation (FRE).

As can be seen in Figure 3.5, the proposed formula gives the exact diagram of flexural rigidity. The differences between this plot and the flexural rigidity diagram obtained from nominal conditions give the location and magnitude of damages along the beam.

3.4.2 Statically Indeterminate System

3.4.2.1 Using Deflection Influence Line (DIL)

Like Example 1, the resultant DIL and its first and second derivatives are plotted in Figure 3.6a–c using a FE model and the CDM. Using this procedure, the diagram of moment $m(\xi)$ is plotted in Figure 3.6d. By using Eq. (3.5), the resultant calculated beam flexural rigidity is presented in Figure 3.6e. As can be seen from Figure 3.6e, the proposed formula was able to predict the flexural rigidity correctly, aside from a small region between locations $x = 3.3$ and $x = 3.7$ where the flexural rigidity curve diverges.

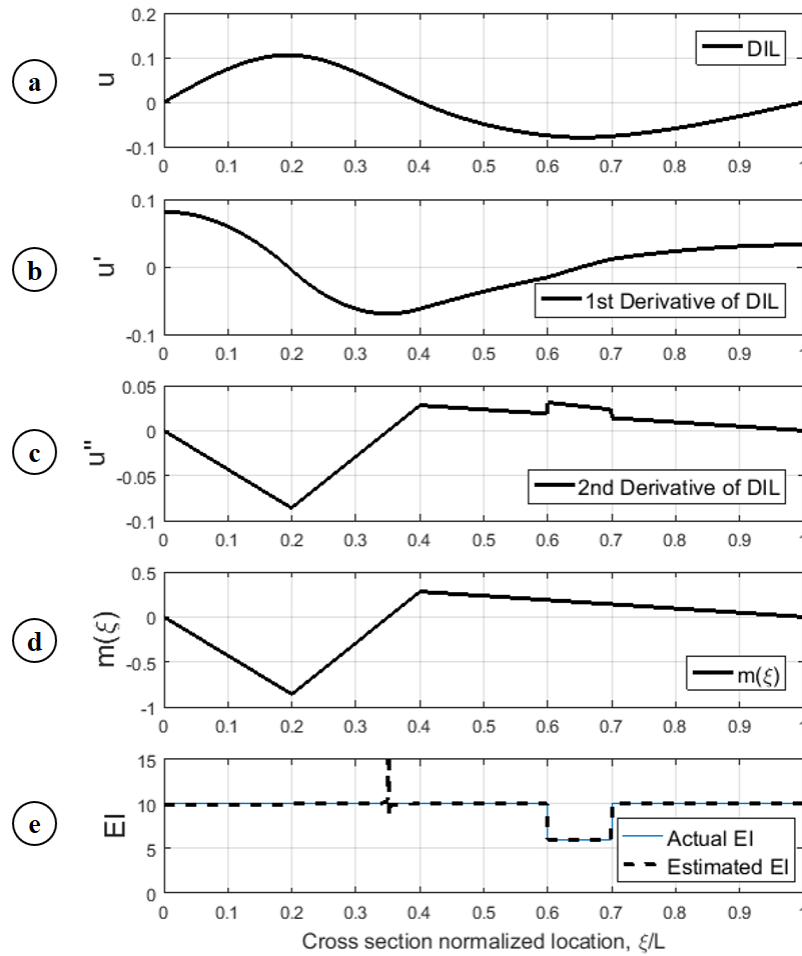


Figure 3.6: Analysis results, (a) Recorded DIL, (b) First derivative of the DIL, (c) Second derivative of the DIL, (d) Diagram of moment $m(\xi)$, and (e) Beam flexural rigidity estimation (FRE).

As stated previously, the proposed formula in Eq. (3.1) is valid when the terms $u''(\xi)$ or $m(\xi)$ are not equal to zero. The ratio of $m(\xi)/u''(\xi)$ is unstable around zero points of $m(\xi)$. Due to the implementation of numerical methods in the calculation of the second derivative, the magnitudes of u'' are not precise enough to give the correct answers near zero values. Consequently, flexural rigidity is not precisely predicted where $m(\xi)$ approaches zero.

3.4.2.2 Using Rotation Influence Line (RIL)

The resultant diagrams for Example 2 when the RIL is utilized are given in Figure 3.7. As can be seen in Figure 3.7e, the RIL was able to correctly predict the flexural rigidity of all cross-sections.

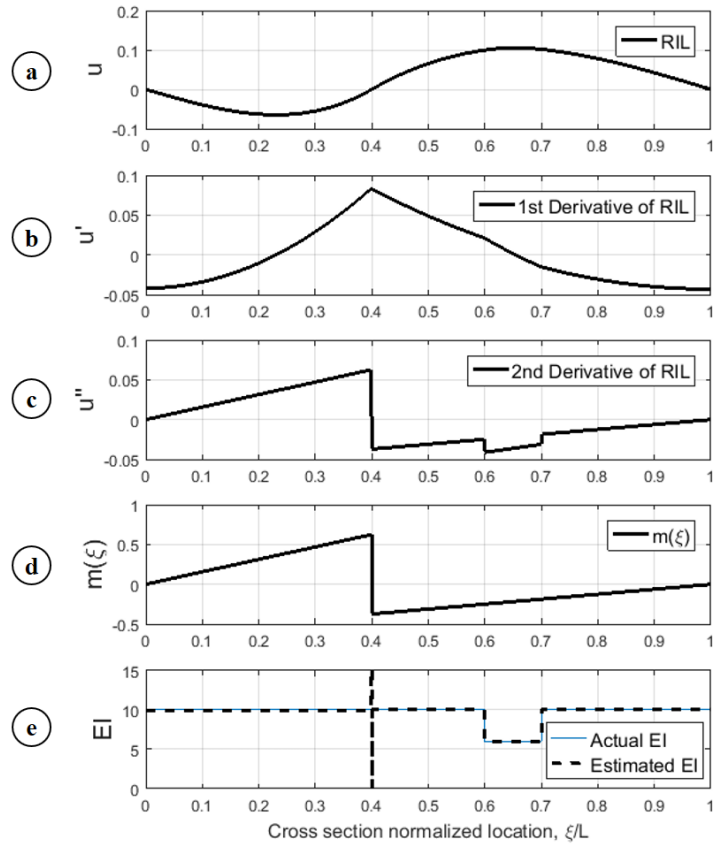


Figure 3.7: Analysis results, (a) Recorded RIL, (b) First derivative of the RIL, (c) Second derivative of the RIL, (d) Diagram of moment $m(\xi)$, and (e) Beam flexural rigidity estimation (FRE).

CHAPTER 4
ANALYTICAL INVESTIGATION USING NOISY INFLUENCE LINE FOR
FLEXURAL RIGIDITY ESTIMATION

4.1 Motivation

In the absence of noise in the recorded data, the finite difference method (FDM) is capable of accurately estimating the second derivative of the influence line and FRE equation gives the exact flexural rigidity. However, in practice, measurement errors are unavoidable and the FDM is unable to construct a useful second derivative of noisy data. The sensitivity of the FRE method to unavoidable noise in deformation measurements necessitates an analysis method robust against such measurement noise.

Multiple methods to overcome the problem of using noisy measurements are presented in this chapter. All of the presented methods are based on a curve-fitting problem in which either a parametric or non-parametric function is fitted to the noisy measurement and the second derivative of the fitted curve is calculated.

4.2 Curve-Fitting Using Parametric/Non-parametric Approximation Method

The considered Euler-Bernoulli beam is linearly elastic and exhibits linear geometric behavior. Without loss of generality, it can be assumed that this beam is divided into a finite number of segments (NS), as illustrated in Figure 4.1, and the flexural rigidity along

each segment is constant and equal to its value at the center of the segment. This segmentation approach resembles the Transfer Matrix Method (TMM) whereby quantities of interest (e.g., forces and displacements) are calculated based on adjacent sections through a sequence of matrix multiplications (Clough & Penzien, 1975; Stephen, 2009). As in the TMM or finite element analysis, a balance should be struck between the number of segments or elements and computational requirements; in the case of damage detection, NS should be chosen such that the rigidity is appropriately affected by the expected damage. In a parametric approximation approach, a function with predefined form and unknown coefficients is fitted to the measured dataset, while in a non-parametric approach, the available information builds up the equation of the fitted curve. The methods presented in this section seek to fit a smooth parametric function to the measured noisy influence line. After curve-fitting, an estimation of the second derivative of the influence line is constructed using this approximated function. The fitted function should be continuous and smooth while closely estimating the numerical values at each measurement.

4.2.1 Moving Window Method

In this method, a series of measurement points are selected and a polynomial function is fitted to them. The number of points can be variable. As will be later presented, increasing the number of points considered in this method increases the certainty level, although the accuracy of the method will decrease. Hence, there exists an optimal solution for the number of considered points.

The assumption behind the moving window method is that the flexural rigidity is constant along each segment. Hence, the right side of Eq. (3.1) remains constant along this

region, i.e., the ratio of the nominator over the denominator remains the same. Consequently, the denominator of Eq. (3.1) should be a linear function like the numerator:

$$u''(x) = \alpha m(x) = \alpha (p(x) + q) \quad (4.1)$$

This means that second derivative of the fitted curve is a first order polynomial. Accordingly, the actual fitted curve is a cubic function. Hence, the shape of the fitted curve in Moving-window method is a cubic polynomial function. Eq. (4.2) presents the basic shape of this fitting curve:

$$u_{MW}(x) = ax^3 + bx^2 + cx + d \quad (4.2)$$

In this equation, coefficients $\{a, b, c, d\}$ are unknowns.

The cost function in this curve fitting problem is:

$$J = \min_{\alpha_{i,j}} \frac{1}{2} \sum_{i=1}^{NM} \|u_{MW}(X_{s_i}) - u_i\|^2 \quad (4.3)$$

By taking the derivative of the cost function with respect to the unknown coefficients and setting the resultant equations to zero, the solution to this curve fitting problem is achieved. The second derivative of the fitted curve is equal to,

$$u''_{MW}(x) = 6ax + 2b \quad (4.4)$$

It can be shown that the solution to this curve fitting problem gives the second derivative as a linear function of measurement points. That means the solution to the second derivative can be rewritten as,

$$u''_{MW}(x) = \sum_{i=1}^{NM} w_{MW_i} u_i \quad (4.5)$$

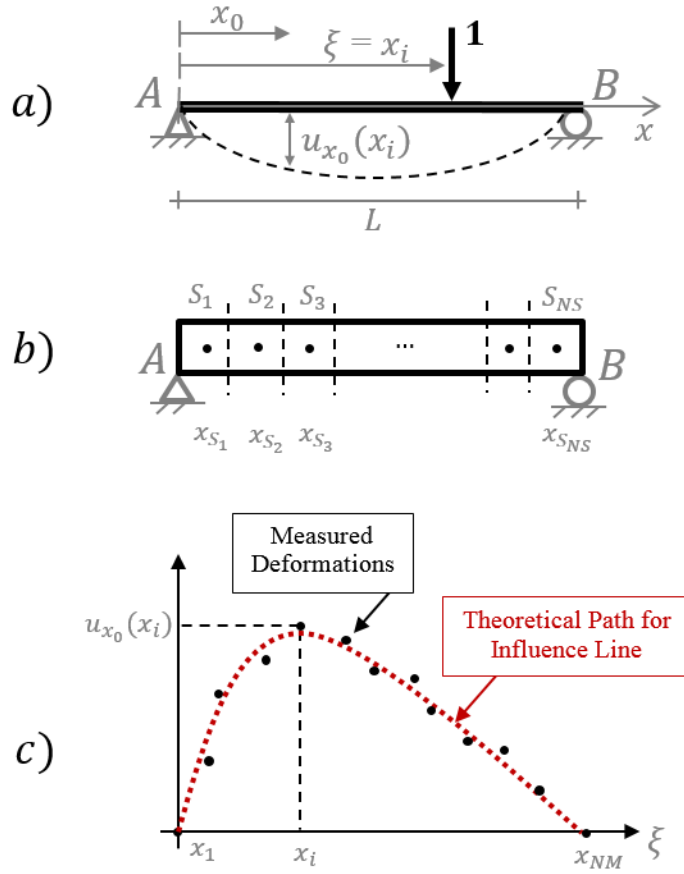


Figure 4.1: (a) A simply-supported beam under the effects of a moving unit load, (b) Beam segmentation and locations of segments' centers (x_{s_i}), (c) Hypothetical illustration of a measured influence line and its theoretical path.

In Eq. (4.5), w_{MW_i} are parameters that are independent of u_i and are calculated based on the solution of the linear curve fitting problem.

4.2.2 Least-mean Square Error (LSQ) Method

In this method, a piecewise cubic spline function is selected as the fitting function. According to the previous section, a cubic function is sufficient for the case of having uniform flexural rigidity along each segment. So, the form of the fitting function is:

for $i \in [1, NS] \rightarrow$

$$u_{LSQ}(x) = u_i(x) = a_i x^3 + b_i x^2 + c_i x + d_i \quad \frac{(i-1)L}{NS} \leq x \leq \frac{iL}{NS} \quad (4.6)$$

In Eq. (4.6), index i varies from 1 to NS . In Eq. (4.6), $u_i(x)$ is the fitted curve to the noisy influence line in segment i . According to the fact that UIL is a deformation influence line, the function $u_{fit.}(x)$ is constrained by the following boundary conditions:

$$\begin{cases} u_1(0) = 0 & \text{(I)} \\ u_{NS}(L) = 0 & \text{(II)} \\ u_i\left(\frac{iL}{NS}\right) = u_{i+1}\left(\frac{iL}{NS}\right) & 1 \leq i \leq NS - 1 & \text{(III)} \\ u'_i\left(\frac{iL}{NS}\right) = u'_{i+1}\left(\frac{iL}{NS}\right) & 1 \leq i \leq NS - 1 & \text{(IV)} \end{cases} \quad (4.7)$$

Boundary conditions (I) and (II) ensure that the fitted curve, the DIL or RIL, starts from zero and finally becomes equal to zero, respectively. Also, continuity equations (III) and (IV) ensure that the fitted curve and its first derivative are continuous and, consequently, the second derivative of this fitted curve exists.

The boundary condition (IV) for all $i \leq NS - 1$ yields:

$$\forall i \leq NS - 1 \rightarrow b_{i+1} = b_i + \frac{2iL}{NS}(a_i - a_{i+1}) \quad (4.8)$$

Also, the boundary condition (III) for all $i \leq NS - 1$ gives:

$$c_{i+1} = c_i + \left(\frac{iL}{NS}\right)^2 (a_i - a_{i+1}) + \left(\frac{iL}{NS}\right) (b_i - b_{i+1}) \quad (4.9)$$

Substituting Eq. (4.9) in Eq. (4.5) yields:

$$\forall i \leq NS - 1 \rightarrow c_{i+1} = c_i - \left(\frac{iL}{NS}\right)^2 (a_i - a_{i+1}) \quad (4.10)$$

Also, the boundary condition (I) gives:

$$u_1(0) = a_1 \cdot 0 + b_1 \cdot 0 + c_1 = 0 \rightarrow c_1 = 0 \quad (4.11)$$

And, boundary condition (II) gives:

$$u_{NS}(L) = a_{NS}L^2 + b_{NS}L + c_{NS} = 0 \rightarrow b_{NS} = -La_{NS} - \frac{1}{L}c_{NS} \quad (4.12)$$

Applying boundary conditions gives that both b_i and c_i are functions of a_i . It follows that once a_i are calculated by solving the curve fitting problem, then c_i and b_i can be calculated as below:

$$c_1 = 0 \quad (4.13)$$

$$\forall 1 \leq i \leq NS - 1 \rightarrow c_{i+1} = c_i - \left(\frac{iL}{NS}\right)^2 (a_i - a_{i+1}) \quad (4.14)$$

$$b_{NS} = -La_{NS} - \frac{1}{L}c_{NS} \quad (4.15)$$

$$\forall NS - 1 \geq i \geq 1 \rightarrow b_{i+1} = b_i + \frac{2iL}{NS}(a_i - a_{i+1}) \quad (4.16)$$

According to Eqs. (4.9)-(4.12), in the curve fitting problem, the vector $\mathbf{a}^T = \{a_1, a_2, \dots, a_{NS}\}$ is the vector of unknowns and vectors $\mathbf{b}^T = \{b_1, b_2, \dots, b_{NS}\}$ and $\mathbf{c}^T = \{c_1, c_2, \dots, c_{NS}\}$ are linear functions of the vector \mathbf{a} and they can be related in a matrix format as $\mathbf{b}^T = \mathbf{B}\mathbf{a}$ and $\mathbf{c}^T = \mathbf{C}\mathbf{a}$. In these relations matrix \mathbf{C} is equal to:

$$\mathbf{C} = \left(\frac{L}{NS}\right)^2 [C_{i,j}]_{NS \times NS} \quad (4.17)$$

Where,

$$C_{i,j} = \begin{cases} i = 1 \rightarrow C_{i,j} = 0 \\ i > 1 \rightarrow \begin{cases} C_{i,j} = -j^2 + (j-1)^2 & i > j \\ C_{i,j} = (i-1)^2 & i = j \\ C_{i,j} = 0 & i < j \end{cases} \end{cases} \quad (4.18)$$

And, matrix \mathbf{B} is equal to:

$$\mathbf{B} = \left(\frac{L}{NS}\right) [B_{i,j}]_{NS \times NS} - \frac{c_{NS}}{L} \quad (4.19)$$

Where,

$$B_{i,j} = \begin{cases} i = NS \rightarrow \begin{cases} B_{i,j} = 0 & j \neq NS \\ B_{i,j} = -NS & j = NS \end{cases} \\ i < NS \rightarrow \begin{cases} B_{i,j} = -2i & j = i \\ B_{i,j} = -2 & i < j < NS \\ B_{i,j} = NS - 2 & j = NS \end{cases} \end{cases} \quad (4.20)$$

Using these definitions, Eq. (4.2) can be rewritten as:

$$\begin{aligned} u_{fit.}(x) &= \mathbf{L}_x(x^2 \mathbf{a} + x \mathbf{b} + \mathbf{c}) = \mathbf{L}_x(x^2 \mathbf{a} + x \mathbf{B} \mathbf{a} + \mathbf{C} \mathbf{a}) \\ &= \mathbf{L}_x \left(\underbrace{(x^2 \mathbf{I} + x \mathbf{B} + \mathbf{C}) \mathbf{a}}_{\mathbf{u}_x} \right) \end{aligned} \quad (4.21)$$

In which, matrix $\mathbf{U}_x \in \mathcal{R}^{NS \times NS}$ and vector $\mathbf{L}_x \in \mathcal{R}^{1 \times NS}$ are functions of new input x and equal to:

$$\mathbf{U}_x = x^2 \mathbf{I} + x \mathbf{B} + \mathbf{C} \quad (4.22)$$

$$\mathbf{L}_x = \{\delta_1, \delta_2, \dots, \delta_{NS}\} = \begin{cases} \delta_i = 1 & \frac{(i-1)L}{NS} < x \leq \frac{iL}{NS} \\ \delta_i = 0 & \text{otherwise} \end{cases} \quad (4.23)$$

This optimization problem can be simplified as a constrained linear least-squares problem, which may be solved by the robust **lsqlin** function implemented in the MATLAB programming software. The constraints and the objective function are defined as linear equations in the format $\mathbf{A}_{cts} \mathbf{X} = \mathbf{b}_{cts}$ and $\mathbf{A}_{obj} \mathbf{X} = \mathbf{b}_{obj}$, respectively, where vector \mathbf{X} is the vector of unknowns. Appendix A presents the method for calculating these matrices. Resultant matrices \mathbf{A}_{obj} , \mathbf{b}_{obj} , \mathbf{A}_{cts} , and \mathbf{b}_{cts} are input into the **lsqlin** function using the ‘‘Interior-Point’’ algorithm (Mathworks, 2017).

It can be shown that the resultant second derivative of from LSQ method is a linear function of all measurement points, as:

$$u''_{TR}(x) = \sum_{i=1}^{NM} w_{LSQ_i} u_i \quad (4.24)$$

In the same way as Eq. (4.5), the parameters w_{LSQ_i} in Eq. (4.24) are all independent from u_i and should be found based the considered parameters in the LSQ method, i.e. number of segment, length of the segments.

4.2.3 Tikhonov Regularization Method

Depending on whether NS is equal to NM or not, the solution of Eq. (4.24) is an over-fitted or an ill-conditioned problem, respectively. A regularizing algorithm provides a technique to transform an ill-posed problem to a well-posed problem and find a stable approximate solution. As stated before, the idea of the regularizing algorithm, which constrains the solution on the smoothness of fitted curve, is based on the implementation of additional information regarding the required solution when the initial *a priori* information is insufficient to give a unique one (Tikhonov et al., 1995).

In the TR method, to ensure the smoothness, an additional term is added to the objective cost function as Eq. (4.25).

$$J_{TR}(\mathbf{a}, \lambda) = \sum_{i=1}^{NM} \frac{1}{2} \left(u_{fit.}(x_i) - u_{x_0}(x_i) \right)^2 + \sum_{i=1}^{NS} \frac{1}{2} \lambda (a_i - a_{i_p})^2 \quad (4.25)$$

In Eq. (4.25), a_{i_p} is the magnitude of a_i when segment- i of beam is intact, i.e. when beam is intact, the vector \mathbf{a} is equal to vector \mathbf{a}_p , and λ is the regularization or smoothness parameter. In the conventional TR, λ controls the smoothness of the solution and is positive.

The least-mean-square solution norm (ρ) and regularization solution norm (η) of Eq. (4.25) are defined as:

$$\rho = \sqrt{\sum_{i=1}^{NM} \frac{1}{2} \left(u_{fit.}(x_i) - u_{x_0}(x_i) \right)^2} \quad (4.26)$$

$$\eta = \sqrt{\sum_{i=1}^{NS} \frac{1}{2} (a_i - a_{iP})^2} \quad (4.27)$$

Minimizing the second term of Eq. (4.25), η , results in a vector \mathbf{a} which gives the flexural rigidity curve of the intact beam. Minimizing both terms in Eq. (4.25) at the same time provides an approximate, but well-posed, solution of vector \mathbf{a} . The parameter λ controls the tradeoff between curve fitting and reducing the norm of the solution (Engl, Hanke, & Neubauer, 1996; Hansen, 1998; Li & Law, 2010; Tikhonov et al., 1995).

Differentiating Eq. (4.25) leads to establishing critical points at which the minima or maxima of the function occur. Hence, the solution of this minimization problem can be expressed as:

$$\frac{\partial J_{TR}(\mathbf{a}, \lambda)}{\partial a_j} = \begin{bmatrix} \frac{\partial J_{TR}}{\partial a_1} \\ \frac{\partial J_{TR}}{\partial a_2} \\ \vdots \\ \frac{\partial J_{TR}}{\partial a_{NS}} \end{bmatrix} = 0 \quad (4.28)$$

Substituting Eq. (4.25) into Eq. (4.28) gives:

$$\frac{\partial J_{TR}}{\partial a_j} = \sum_{i=1}^{NM} (u_{fit}(x_i) - u_A(x_i)) \frac{\partial u_{fit}(x_i)}{\partial a_j} + \sum_{i=1}^{NS} \lambda (a_i - a_{iP}) \frac{\partial a_i}{\partial a_j} = 0 \quad (4.29)$$

In Eq. (4.29),

$$\frac{\partial a_i}{\partial a_j} = \delta(i - j) = \begin{cases} 1 & i = j \\ 0 & i \neq j \end{cases} \quad (4.30)$$

Also, utilizing Eq. (4.22) and Eq. (4.23) gives,

$$\frac{\partial u_{fit}(x_i)}{\partial a_j} = \frac{\partial (\mathbf{L}_{x_i}(\mathbf{U}_{x_i} \mathbf{a}))}{\partial a_j} = \mathbf{L}_{x_i} (\mathbf{U}_{x_i} \delta(i - j)) = \mathbf{L}_{x_i} \mathbf{U}_{x_i}(:, j) \quad (4.31)$$

In which, $\mathbf{U}_{x_i}(:, j)$ is the j -th column of matrix \mathbf{U}_{x_i} . Expanding Eq. (4.28) for each j gives:

$$\underbrace{\sum_{i=1}^{NM} u_{fit.}(x_i) \frac{\partial u_{fit.}(x_i)}{\partial a_j}}_{(I)} + \underbrace{\sum_{i=1}^{NS} \lambda a_i \frac{\partial a_i}{\partial a_j}}_{(II)} = \underbrace{\sum_{i=1}^{NM} u_A(x_i) \frac{\partial u_{fit.}(x_i)}{\partial a_j}}_{(III)} + \underbrace{\sum_{i=1}^{NS} \lambda a_{i_p} \frac{\partial a_i}{\partial a_j}}_{(IV)} \quad (4.32)$$

Where,

$$(I) = \sum_{i=1}^{NM} [\mathbf{L}_{x_i}(\mathbf{U}_{x_i} \mathbf{a})][\mathbf{L}_{x_i} \mathbf{U}_{x_i}(:, j)] = \left(\sum_{i=1}^{NM} [\mathbf{L}_{x_i} \mathbf{U}_{x_i}][\mathbf{L}_{x_i} \mathbf{U}_{x_i}(:, j)] \right) \mathbf{a} = k_j \mathbf{a} \quad (4.33)$$

$$(II) = \sum_{i=1}^{NS} \lambda a_i \delta(i - j) = \lambda a_j \quad (4.34)$$

$$(III) = \sum_{i=1}^{NM} u_A(x_i) [\mathbf{L}_{x_i} \mathbf{U}_{x_i}(:, j)] = F_j \quad (4.35)$$

$$(IV) = \sum_{i=1}^{NS} \lambda a_{i_p} \delta(i - j) = \lambda a_{j_p} \quad (4.36)$$

Hence, for each j , Eq. (4.32) can be simplified as:

$$k_j \mathbf{a} + \lambda a_j = F_j + \lambda a_{j_p} \quad (4.37)$$

Therefore, putting together entire NS equations that are achieved from Eq. (4.28) gives:

$$(\mathbf{K} + \lambda \mathbf{I}) \mathbf{a} = \mathbf{F} + \lambda \mathbf{a}_p \quad (4.38)$$

In which,

$$\mathbf{K} = \begin{bmatrix} k_1 \\ k_2 \\ \vdots \\ k_{NS} \end{bmatrix}_{NS \times NS} \rightarrow [k_j]_{1 \times NS} = \sum_{i=1}^{NM} [\mathbf{L}_{x_i} \mathbf{U}_{x_i}][\mathbf{L}_{x_i} \mathbf{U}_{x_i}(:, j)] \quad (4.39)$$

$$\mathbf{F} = \begin{bmatrix} F_1 \\ F_2 \\ \vdots \\ F_{NS} \end{bmatrix}_{1 \times NS} \rightarrow [F_j]_{1 \times 1} = \sum_{i=1}^{NM} u_A(x_i) [\mathbf{L}_{x_i} \mathbf{U}_{x_i}(:, j)] \quad (4.40)$$

Accordingly, Eq. (4.28) is rewritten as:

$$(\mathbf{K} + \lambda \mathbf{I}) \mathbf{a} = \mathbf{F} + \lambda \mathbf{a}_p \quad (4.41)$$

In Eq. (4.41), matrices \mathbf{K} , \mathbf{F} , and \mathbf{a}_p are known and matrix \mathbf{I} is the identity matrix. Eq. (4.41) gives the solution for vector \mathbf{a} as:

$$\mathbf{a} = (\mathbf{K} + \lambda \mathbf{I})^{-1} (\mathbf{F} + \lambda \mathbf{a}_p) \quad (4.42)$$

The regularization parameter λ primarily controls the smoothness of approximated function; increasing the parameter λ increases the smoothness of the approximated curve for flexural rigidity. The regularization parameter, λ , can be determined using one of the methods below:

- The generalized cross validation method (Golub, Heath, & Wahba, 1979)
- The L-curve criterion (Hansen, 1992)
- Morozov discrepancy principle technique (Pereverzev & Schock, 2000)

No singularly preferred approach exists for all situations (Ranjbar, 2010); the L-curve method is utilized to determine the best value of smoothing parameter in this study.

The L-curve diagram is a log-log scale plot of η versus corresponding ρ , for all valid regularization parameters. This plot illustrates the compromise between the two considered norms in the objective function. The plot has an L-shape appearance with a distinct corner that separates the vertical and horizontal legs where the regularization solution and the least-mean-square norm are more sensitive to λ , respectively. According to the L-curve method, the regularization parameter that gives the highest positive

curvature in the L-curve plot (i.e. L-curve corner), is selected as the optimal λ (Hansen, 1998; Hansen & O’Leary, 1993; Li & Law, 2010). It is clear that, from data in this study, the valid solution to this one-dimensional optimization of λ is a value that gives positive EI_i less than or equal to EI_{i_p} , the maximum possible flexural rigidity in segment- i .

It can be shown that, in opposite to the LSQ method, the TR method does not give a linear relation between the second derivative and the magnitude of the measurement. So, this relation can be presented by:

$$u''_{TR}(x) = \sum_{i=1}^{NM} \left(w_{TRi} + \lambda(U_1, \dots, U_{NM}) \right) U_i \quad (4.43)$$

4.3 Performance Optimization of the Methods

Whenever a new model is proposed, its applicability and superiority to the existing models should be presented in a clear and statistically meaningful manner. Accordingly, each new method should be benchmarked under optimal conditions on available analytical and experimental data sets; all hyper parameters of each method should be optimized.

To find an optimal solution to each method such that the methods can be compared, a unique objective function is considered for each method and each method’s hyper parameters should be optimized according to the objective function. The optimal solution to the FRE problem is a function with the level of the accuracy required for practical implementation. Assume that the second moment of area (I) is to be calculated within a limit (ΔI). So,

$$I_{predicted} = I_{system} \pm \Delta I \quad (4.44)$$

Or,

$$\varepsilon_I = \pm \frac{\Delta I}{I_{system}} \quad (4.45)$$

Where, ε_I defines the level of the accuracy of the predicted I . Accordingly, the objective function is to reach to optimal value for hyper parameters in a way that method predicts the I with less than selected ε_I .

To formulate this objective function, the relationship between the ε_I and the method hyper parameters is investigated.

To find the relationship between ΔI and $\Delta u''$, Eqs. (3.1) and (4.45) are substituted into Eq. (4.44)

$$I_{predicted} = \frac{m(x)}{u''_{system}(x)} (1 \pm \varepsilon_I) \quad (4.46)$$

In the same manner, it can also be shown that,

$$I_{predicted} = \frac{m(x)}{u''_{predicted}(x)} = \frac{m(x)}{u''_{system}(x)(1 \pm \varepsilon_{u''})} \quad (4.47)$$

Hence,

$$\frac{m(x)}{u''_{system}(x)} (1 \pm \varepsilon_I) = \frac{m(x)}{u''_{system}(x)(1 \pm \varepsilon_{u''})} \quad (4.48)$$

Assuming, $\frac{m(x)}{u''_{system}(x)} \neq 0$, gives:

$$1 \pm \varepsilon_I = \frac{1}{1 \pm \varepsilon_{u''}} = \frac{1 \mp \varepsilon_{u''}}{(1 \pm \varepsilon_{u''}) \times (1 \mp \varepsilon_{u''})} = \frac{1 \mp \varepsilon_{u''}}{1 - \varepsilon_{u''}^2} \quad (4.49)$$

In Eq. (4.49), if $\varepsilon_{u''} < 0.1$, then it follows that $1 - \varepsilon_{u''}^2 > 0.99$; thus, it can be assumed that $1 - \varepsilon_{u''}^2 \cong 1$, and

$$\varepsilon_I = \varepsilon_{u''} = \frac{\Delta u''}{u''_{system}(x)} \quad (4.50)$$

The parameter u''_{system} is a fixed value at each point of the system and not a variable of existing noise. So, the parameter $\Delta u''$ is optimized and is equal to

$$u''_{measured} = u''_{system} \pm \Delta u'' \quad (4.51)$$

The same relation exists for the influence line measurement, as:

$$u_{measured} = u_{system} \pm \Delta u \quad (4.52)$$

Assuming that the measurement sensor is the only source of noise, the parameter Δu is a predefined known fixed value that depends on the sensor. Moreover, each method defines the relation between the Δu and $\Delta u''$. Accordingly, by knowing the value of Δu , the hyper parameters of each method should be find in a way that gives, the resultant ε_l or equivalently $\varepsilon_{u''}$, remains within the desired range.

As stated before, the Moving-window method and the LSQ method each represent a linear relationship between $u_{measured}$ and the u'' . So,

$$u'' = \sum w_i u_i \quad (4.53)$$

Utilizing Eq. (4.53),

$$\Delta u'' = \sum |w_i| \Delta u_i \quad (4.54)$$

And, because Δu is the same for all measurement points, so, in case of having a linear relation,

$$\Delta u'' = \Delta u \sum |w_i| \quad (4.55)$$

In another words, the optimization process should find the optimal value of the hyper parameters such that,

$$\sum |w_i| \leq \varepsilon_{lreq.} \left(\frac{u''_{system}}{\Delta u} \right) \quad (4.56)$$

In Eq. (4.56), the parameter $\varepsilon_{I_{req}}$ is the required level of accuracy for estimated flexural rigidity.

The TR method, gives a nonlinear relationship. Although, it has been shown that (CITATION) that the final solution to the Tikhonov Regularization problem, is not sensitive to the variation of the smoothing parameter around its optimal value (Tikhonov, A. N., Goncharsky, A. V., Stepanov, V. V., & Yagola, A. G. (1995)). Accordingly, it has been assumed that the variation of optimal value for smoothing parameter (λ) for small variations in measurement is negligible and a linear relationship for TR can be considered.

After the optimization of the defined objective function and finding the optimal value for all hyper parameters of each method, the results of the methods become comparable.

4.4 FRE Using the Weighted Average of the Influence Lines

Even after fitting a smooth curve to noisy data, some estimation error will remain in the calculation of the second derivative. Moreover, the FRE is more sensitive to the second derivative calculation error in regions with small values from the unit moment curve; this occurs because the second derivative approaches small values in the denominator of Eq. (3.1). To overcome this challenge, multiple measurements of influence line were recorded, and a weighted average of the results is used, as:

$$EI_{ave.} = \frac{m_{\theta_A}(\xi)}{\theta_A''(\xi)} \cdot f_A + \frac{m_{\theta_B}(\xi)}{\theta_B''(\xi)} \cdot f_B \quad (4.57)$$

where

$$f_A = \left(\frac{L-\xi}{L}\right)^2 \quad (4.58)$$

and

$$f_B = \left(\frac{\xi}{L}\right)^2 \quad (4.59)$$

Eq. (4.57) gives the weighted average of the calculated flexural rigidity from each RIL. In Eq. (4.57), f_A and f_B are the weights. These weights are selected in a way that calculated values for flexural rigidity method gives values closer to the prediction using rotation at support A, at locations closer to support A, and vice versa for the prediction based on the rotations at support B.

4.5 Analytical Modeling

In the investigation of the optimization of each method, a randomly generated dataset of a data streams is used as input to each proposed method and the result of each method is scored based on its closeness to the actual result. At the end, the average of the scores are calculated and the performance of each method is evaluated based on the calculated average. This repeated random validation approach ensures statistically meaningful analyses (Li & Law, 2010).

There are several sources for noise in the influence line measurement. Without the loss of generality, it can be assumed that the existing noise has a normal standard distribution. Accordingly, adding a random noise with standard Gaussian distribution to the actual value of the measurement, can generate one possible instance of noisy measurement. To reach to a statistically meaningful results, this process should be repeated several times, and the average is justified.

In this section, two damage case scenarios for the beam as depicted in Figure 4.2 are considered. In this investigation, only the rotation influence lines at support A are selected as the measured deformation influence lines. Hence, a finite element (FE) model is utilized

to simulate these scenarios and calculate the rotation influence line (*RIL*) at the left support (θ_A) under the effects of a moving unit load. Impairments are modeled by reducing the flexural rigidity at the damaged regions by 40%. In these examples, the monitoring location is kept constant for each analysis.

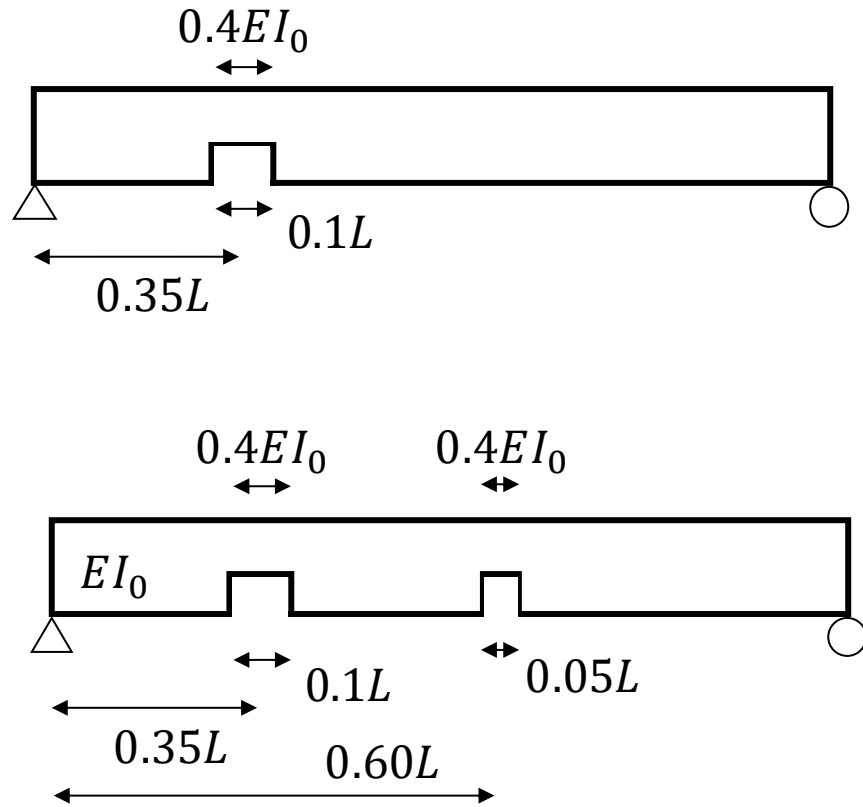


Figure 4.2 Considered Damaged Case Scenarios (a) Case 01 (b) Case 02

To simulate noisy measurements (θ_{noisy}), normally distributed random noise is added to the influence lines ($\theta_{calculated}$) calculated from FE models as:

$$\theta_{noisy} = \theta_{calculated} + \varepsilon_{\theta} \cdot \mathbf{N} \cdot rms(\theta_{calculated}) \quad (4.60)$$

In Eq. (4.60), ε_{θ} is the random noise level; \mathbf{N} is a standard normally distributed random vector with a mean equal to zero and unit standard variance; and $rms(\theta_{calculated})$ is the

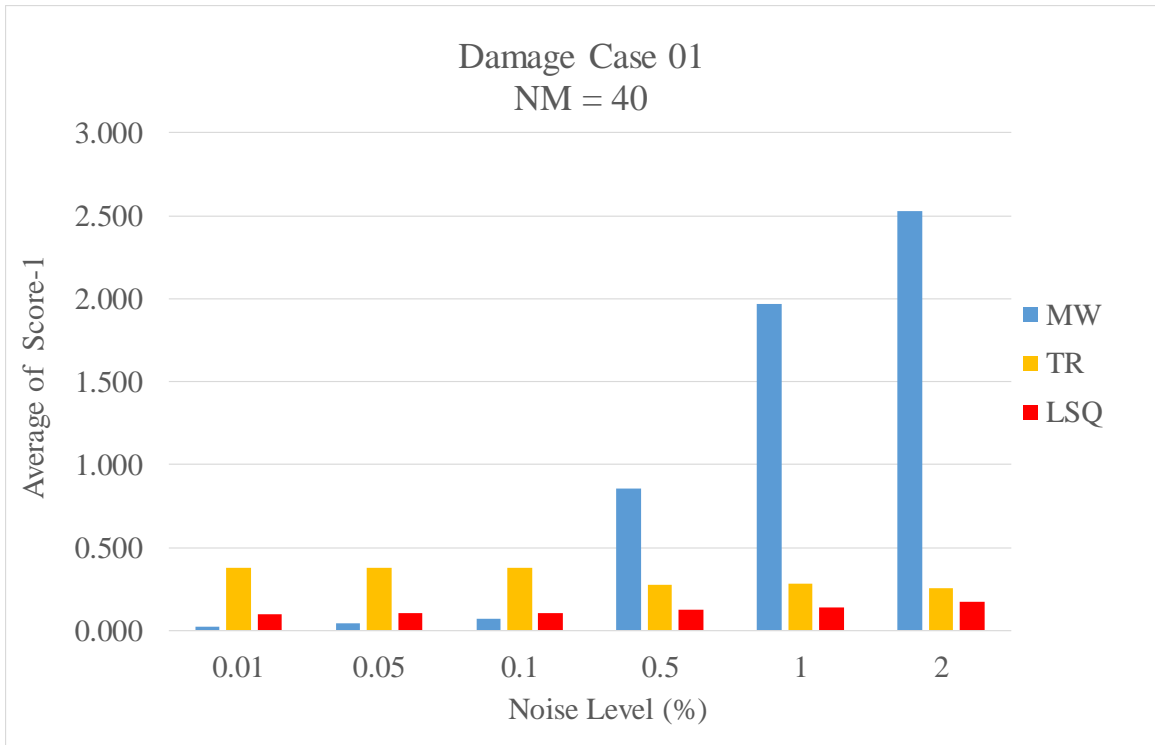
root-mean-square of the calculated RIL. Three number of measurements (NM) equal to 40, 50, and 100, and six levels of noise (NL) equal to 0.01%, 0.05%, 0.1%, 0.5%, 1%, and 2% are considered. Per each configuration of NM and NL, 100 sample of noisy RILs are generated and the optimal solution of the MW, LSQ, and TR methods are calculated. Eventually, the score equation given below is calculated per each method.

$$SCORE_{E_1} = \frac{1}{n} \sum_{i=1}^n \left| \frac{EI_{predicted}(\text{Segment} - i)}{EI_{actual}(\text{Segment} - i)} - 1 \right| \quad (4.61)$$

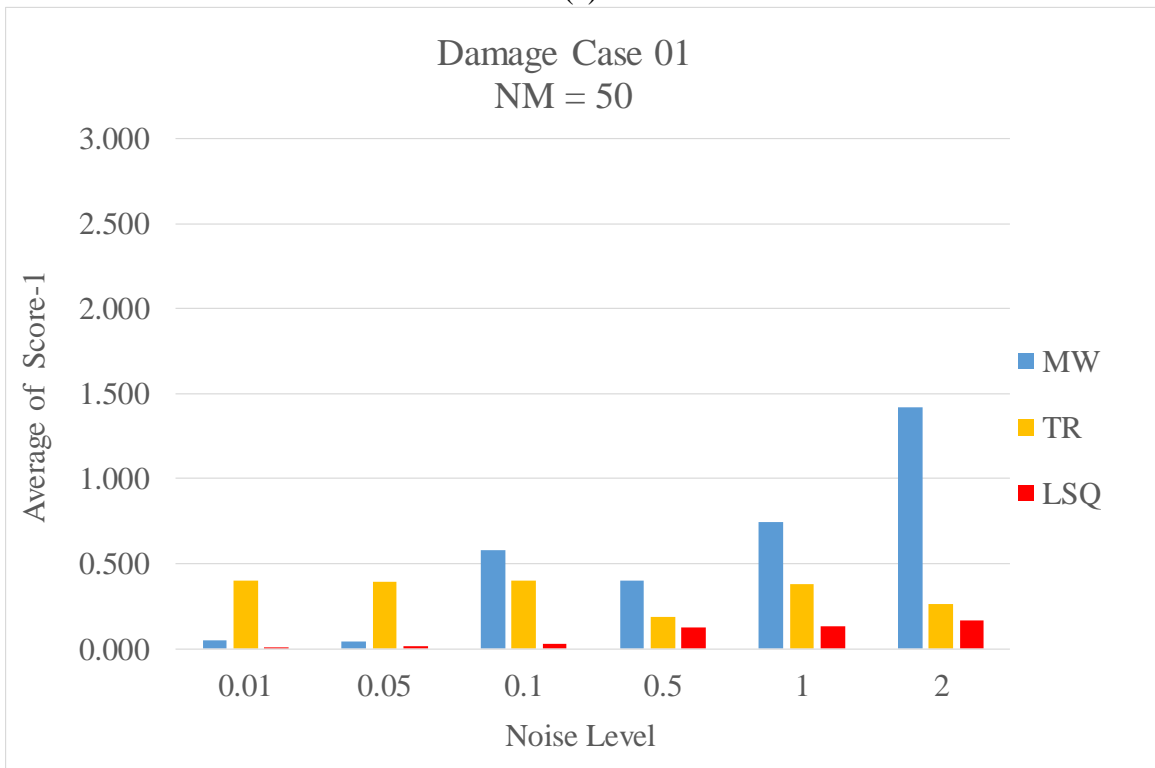
According to this definition, the method with lower score performs better than one that has higher score. At the end, the average of the 100 *SCORE* values is calculated and considered as the performance of each method. Section 4.6 presents the results of this study.

4.6 Analytical Results and Discussion

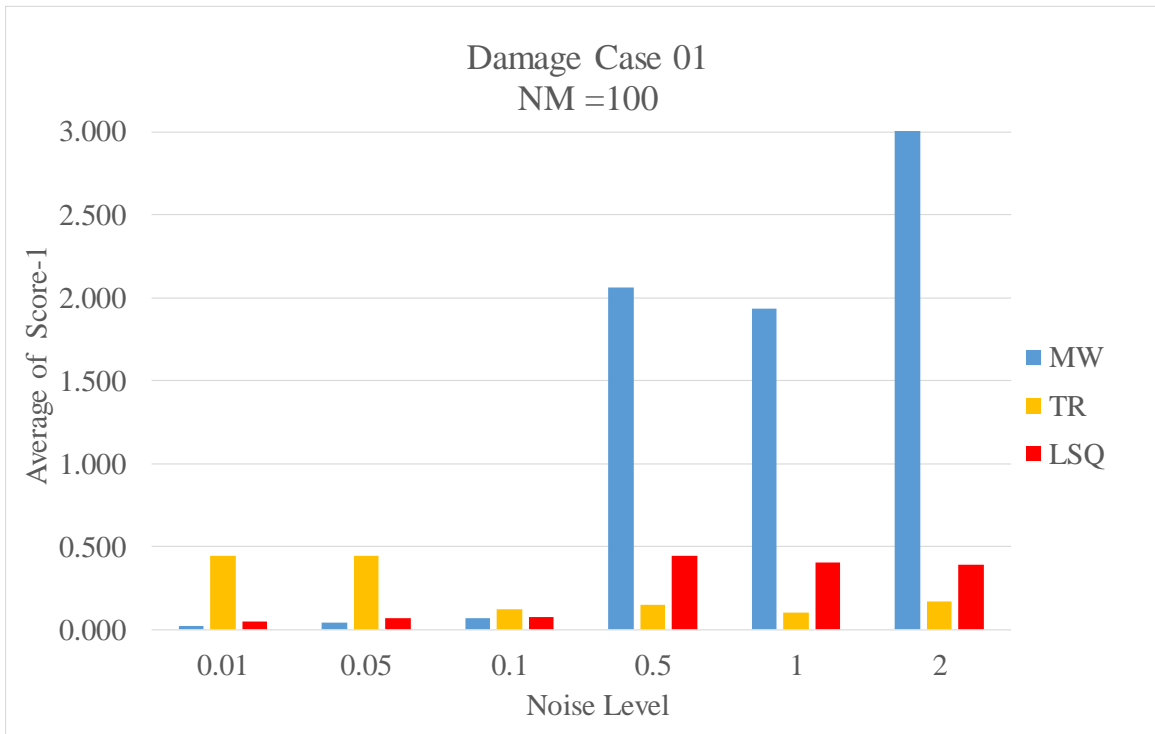
Figure 4.3 and Figure 4.4 illustrate the results of the analytical study. From Figure 4.3a it can be concluded that MW gives the best performance among these three methods at lower noise levels, although, the performance decreases with increasing noise level. The TR and LSQ methods exhibit more consistent results among different noise levels compared to MW, even with increasing noise.



(a)



(b)



(c)

Figure 4.3: Damage Case 01, (a) $NM = 40$, (b) $NM = 50$, (c) $NM = 100$.

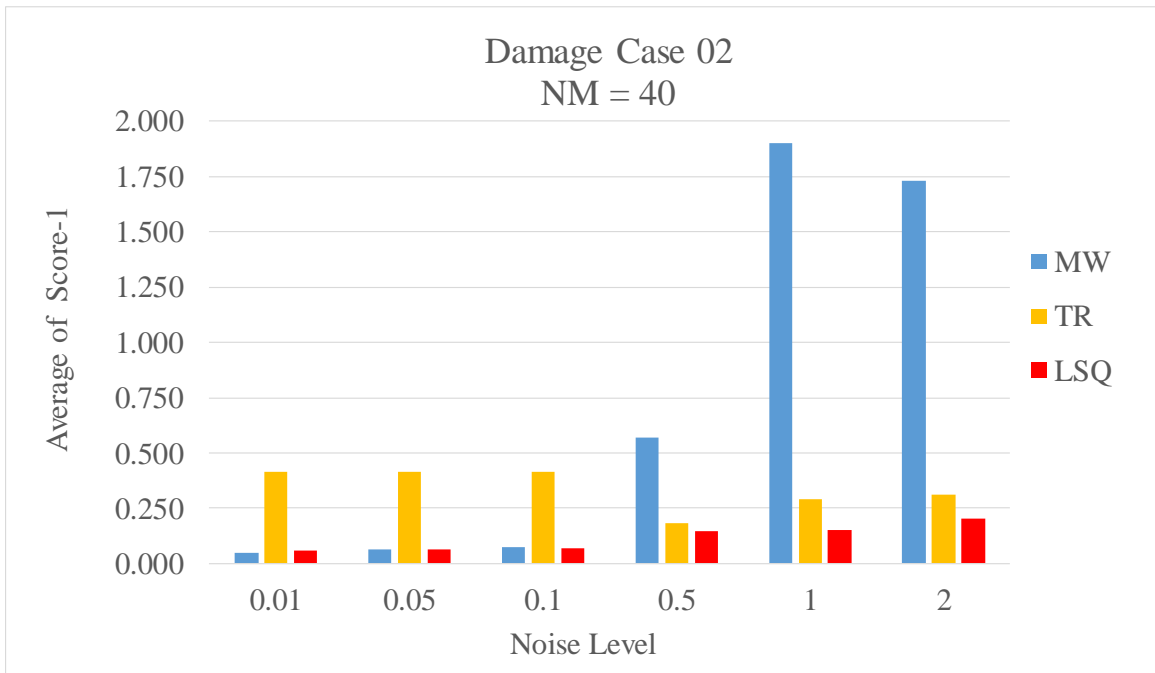


Figure 4.4: Damage Case 02, $NM = 40$.

For lower values of number of measurements, the LSQ performs better than the other two methods, even in higher noise levels. Once both the noise level and the number of measurements increase, i.e., $NM=100$ and $NL = 0.5\%$, 1.0% , or 2.0% , the TR method acts the best among these three methods.

CHAPTER 5

EXPERIMENTAL STUDIES

5.1 General Procedures

In this chapter, the application of the proposed method on three experimental setups is presented. In all experiments, a concentrated load is passed over the entire beam span, stopping at multiple known locations, and the corresponding beam rotation at specific points of the system is measured. Then, by dividing the resultant measured rotation by the magnitude of the applied load, the unit load influence line of the beam rotation is extracted. In all three experiments, a machine vision method with a camera-target setup is utilized for rotation measurement. In the last experiment, a research-grade tilt-meter is also used to capture the rotations.

5.1.1 Camera-Based Data Acquisition

A target-based machine vision system for measuring the 2D movement of a moving object through implementation of a charge-coupled device (CCD) camera and the camera calibration technique proposed by Zhang (Z. Zhang, 2000) is utilized. This refined system achieves higher accuracy compared with current monocular machine-vision systems and avoids the complicated image synchronization and feature-matching processes which are required in stereo-vision applications (C. C. Chang & Xiao, 2010). In the presented system, measurements can be conducted automatically without any additional adjustments after

one-time mounting of the targets and calibration of the camera. The results show that the level of the accuracy is sufficient to satisfy performance metrics in rotations measurement.

5.1.1.1 Theoretical Framework

The projection of the image of a real point on an image plane relies on the physical characteristics of the camera and lens. The goal of a camera calibration technique is to find these physical characteristics. Each camera calibration technique is based on a specific projection model. This section presents the utilized projection model, camera calibration technique, and its corresponding implementation details in this study.

A digital image is a collection of the projections of real-world spatial points. During the physical phenomenon of projection, an optical ray from a 3D point $\mathbf{P} = [X, Y, Z]^T$ passes through the camera optical center and intersects the camera sensor plane to form a 2D image point denoted by $\mathbf{p} = [u, v]^T$. The Modified Pinhole Imaging (MPI) model, a theoretical model for modeling this image projection, is utilized in the proposed CVMM system (Tsai, 1986; Z. Zhang, 2000). There are multiple unknown parameters in the MPI model that require calibration. A common and robust calibration technique is Zhang's camera calibration (ZCC) technique, which was initially introduced by Zhang in 1999 (Z. Zhang, 2000) and has been developed extensively during last couple of decades. This technique iteratively finds and calibrates the unknown parameters within the MPI model. A brief description of the algorithm and implemented notations of the ZCC technique is presented in this section.

A simplified or naive pinhole model, illustrated in Figure 5.1, is only an approximation of the real projection phenomena. While this model allows for a simple mathematical formulation of the relationship between the camera coordinate system (indicated by

subscript C) and the world coordinate system (indicated by subscript W), this model does not achieve a high level of accuracy; more comprehensive camera models can increase accuracy (Jain, Kasturi, & Schunck, 1995). Typically, the simplified pinhole model serves as the basis that is extended with modifications to provide a more comprehensive projection model that systematically considers the image distortions (Z. Zhang, 2000).

In the simplified illustration shown in Figure 5.1, the image plane is positioned between the scene point and the optical center, when in reality the image plane is located on the opposite side of the optical center. The simplified pinhole model does not consider the possibility of distortion in the projection; a nonlinear distortion model is considered in the MPI model (J. Heikkila & Silven, 1997).

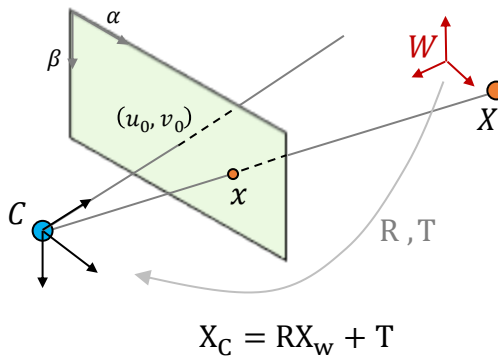


Figure 5.1: Simplified pinhole imaging model.

There are two reference coordinate systems in the MPI model: (1) the world coordinate system (W), which is based on target location, and (2) the camera coordinate system (C). In the MPI model, the location of the projection of the real-world point onto the image plane is calculated as:

$$\mathbf{p} = \begin{bmatrix} u \\ v \end{bmatrix} = \underbrace{\begin{bmatrix} f_x & 0 & u_0 \\ 0 & f_y & v_0 \end{bmatrix}}_A \begin{bmatrix} x_d \\ y_d \\ 1 \end{bmatrix} \quad (5.1)$$

In Eq. (5.1), the matrix A is the intrinsic matrix that contains the effective focal lengths, (f_x, f_y) , and the principal point, (u_0, v_0) . Vector $[x_d \ y_d \ 1]$, a 3×1 vector in Eq. (5.1), contains distorted pixels that are calculated by using the Plumb Bob distortion model. This model was first introduced by Brown in 1966 (Brown, 1966) as:

$$\begin{bmatrix} x_d \\ y_d \end{bmatrix} = \begin{bmatrix} x_n \\ y_n \end{bmatrix} (1 + k_1 r^2 + k_2 r^4 + k_3 r^6) + d_x \quad (5.2)$$

In Eq. (5.2), the terms inside the parentheses are the radial distortion amplifications. If radial distortion is present, light beams bend more at the boundary of the lens than at the principal point. Depending on the direction of the radial distortion curvature, two types of radial distortion may be observed: pincushion distortion or barrel distortion. Vector d_x in Eq. (5.2) is the tangential distortion due to imperfect centering of the lens components (Bouguet, 2000).

Considering two coefficients is usually sufficient for modeling the radial distortion unless a severe distortion exists (Z. Zhang, 2000). Since the lenses of the camera used in this study are parallel to the camera imaging plane, e.g. the CCD, tangential distortion is minimal (Bouguet, 2000; Z. Zhang, 2000). Therefore, the tangential distortion can be neglected and only the radial distortion with two terms, i.e. $(1 + k_1 r^2 + k_2 r^4)$, is considered in this study.

The normalized points $[x_n \ y_n]$ and the r value in Eq. (5.2) are calculated based on the position of the point in the camera coordinate system as:

$$\begin{bmatrix} x_n \\ y_n \end{bmatrix} = \begin{bmatrix} X_c/Z_c \\ Y_c/Z_c \end{bmatrix} \quad (5.3)$$

$$r^2 = x_n^2 + y_n^2 \quad (5.4)$$

where subscript C denotes the camera coordinate system. Transformation of the position of points from the W coordinate system to the C coordinate system is expressed as:

$$\mathbf{P}_C^T = \begin{bmatrix} X_c \\ Y_c \\ Z_c \end{bmatrix} = [R \ T] \begin{bmatrix} X_W \\ Y_W \\ Z_W \\ 1 \end{bmatrix} \quad (5.5)$$

where subscript W denotes the world coordinate system. Matrix $[R \ T]$ in Eq. (5.5) is the extrinsic matrix that contains a 3×3 rotation matrix R and a 3×1 translation vector T .

Eqs. (5.3)-(5.5) include the unknown parameters in the MPI model which can be found using the ZCC technique. The primary steps in the ZCC technique include finding the closed-form solution for the unknown parameters (excluding lens distortion), refining the solution using the maximum-likelihood estimation, and updating the solution accounting for lens distortion.

Assuming a simplified pinhole model excluding possible distortion and calculating the reprojection of the target using this model, each image of the target gives two homogenous equations as a function of unknown intrinsic parameters (Burger, 2016). The ZCC technique states that if three or more images of the target are acquired, then a unique analytical solution defined up to a scale factor exists for all unknown parameters excluding the lens distortion parameters (Z. Zhang, 2000). This analytical solution can be obtained from a linear closed-form solution; however, the initial linear computation is not sufficient to retrieve the accurate mapping between image points and corresponding real points.

The second step attempts to refine this initial linear solution through a maximum-likelihood estimation of the reprojection error (RE). The reprojection error can be defined as:

$$\text{RE} = \sum_{i=1}^N \sum_{j=1}^{M_i} \|x_{i,j} - F(A, R_i, T_i, X_{i,j})\| \quad (5.6)$$

where the function $F(A, R_i, T_i, X_{i,j})$ projects the target spatial points $X_{i,j}$ onto the image plane, $x_{i,j}$. This error is calculated over N images of the target. Each image contains M_i points. The purpose of the refinement in the second step is to minimize the reprojection error that is defined in Eq. (5.6). This nonlinear minimization problem is solved using the Levenberg–Marquardt optimization method. The analytical solution calculated in the first step is used as the initial guess for this optimization problem.

Once the optimal solution for A and $[R_i|T_i]$ per each image is achieved, Eq. (5.6) is updated to include the effects of the lens radial distortion on the camera model. To this end, a modified projection function $\hat{F}(A, K, R_i, T_i, X_{i,j})$, which considers the effects of lens distortion, is used to replace the projection function $F(A, R_i, T_i, X_{i,j})$ in Eq. (5.6). Vector K includes the parameters that define the distortion model. This study includes radial lens distortions that cause the actual image points to be displaced radially in the image plane (J. Heikkila & Silven, 1997).

The ZCC technique implemented in this study utilizes a planar target. A planar target is a target with coplanar features, for example black and white checkerboards. In a planar target, all features, such as corner locations on a checkerboard target, are located on the same plane, and the Z-component of each detected feature is equal to zero in the world coordinate system. Utilization of a target with planar features reduces the number of unknown parameters while camera calibration (Z. Zhang, 2000). The target planarity is important in the ZCC technique, and the existence of any warping in the target decreases

the accuracy of the CVMM system. Prior literature recommends the use of an accurate printer and a rigid, flat mounting surface to create a high-quality planar target (Bouguet, 2000; Burger, 2016; J. Heikkila & Silven, 1997; Z. Zhang, 2000). An example planar target is shown in Figure 5.2.

The extrinsic parameter matrix, $[R|T]$, gives the position and orientation of the camera with respect to the target. The relative spatial information of the camera with respect to the target is determined from the extrinsic parameters. The accuracy and reliability of the extrinsic parameters of each image is a function of the reprojection error, RE .

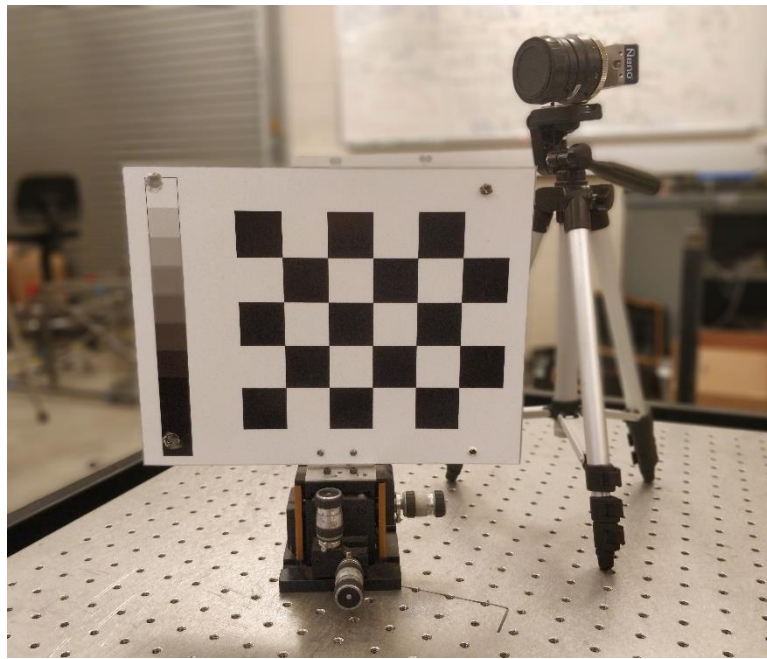


Figure 5.2: Checkerboard target.

5.2 Determinate Beam

5.2.1 Procedure

A rectangular steel specimen with 1.5 mm nominal thickness and 25.4 mm nominal width is supported on the edge of an L-shape bracket in a simply supported manner, as illustrated in the Figure 5.3. A geometrical impairment is created on this specimen by

reducing the cross-section at the specified location in Figure 5.4. The geometry of this simply supported beam and considered nominal values for this experiment are illustrated in Figure 5.4.

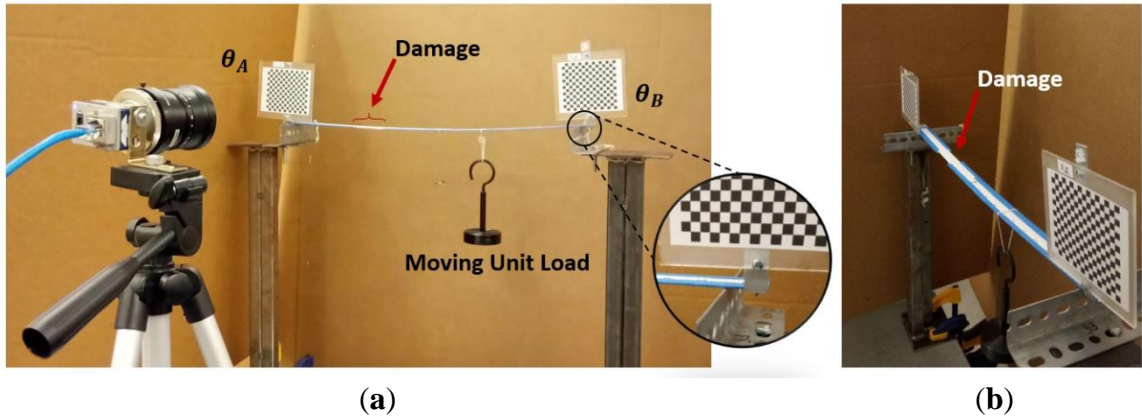


Figure 5.3: Experimental setup, (a) Front view, (b) Side view.

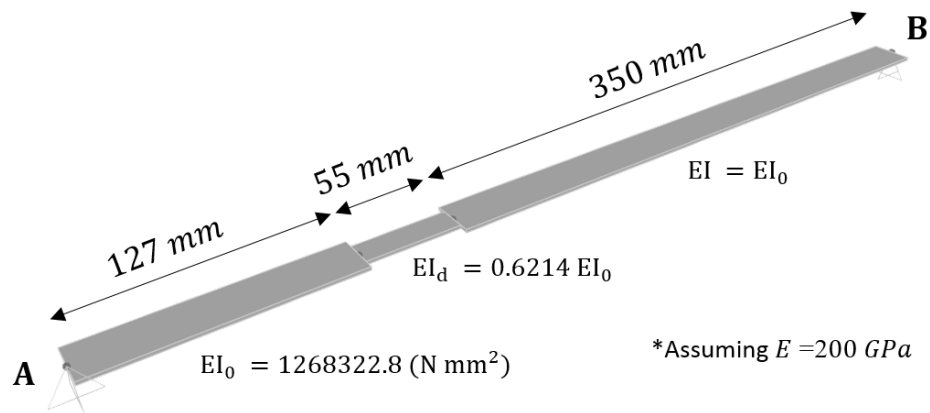


Figure 5.4: Cross-section reduction on the specimen.

The unit RIL was created by measuring rotations at both supports, caused by passing a hanging load of 0.5 kg weight over the beam span with the resolution of 6 mm distance (i.e., totally 81 measurements). Measurements were conducted in a static manner.

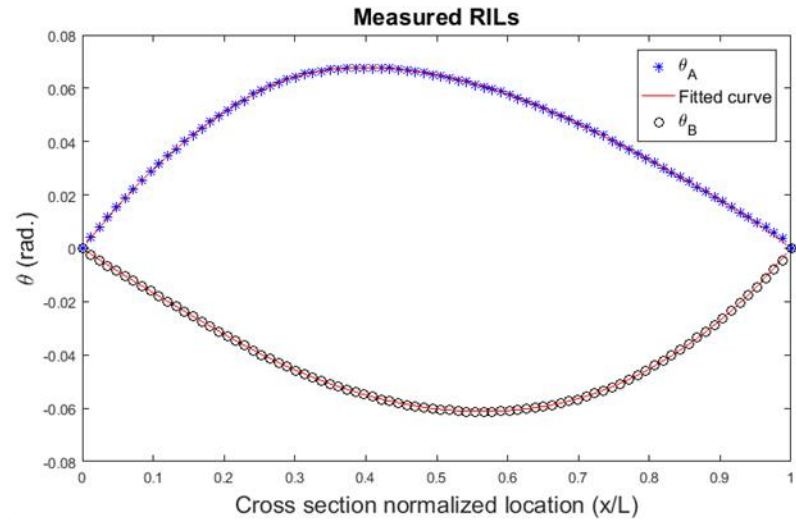
The rotation measurements are conducted by using a machine vision algorithm that is implemented in MATLAB and a robust camera calibration method that tracks the

checkerboards that are attached to the ends of this beam. A camera with a resolution of 2592×2048 pixels, a 75 mm lens, and 15×16 checkerboards with 4.8×4.8 mm squares are utilized for this experiment setup. The RILs at the ends of this simply supported beam are calculated by tracking the movements of the checkerboards corners while the load is moved along the beam span. Zeinali et al. (2017) present the details of this robust measurement method. One advantage of a camera-based displacement estimation is that the location of the load is simultaneously estimated.

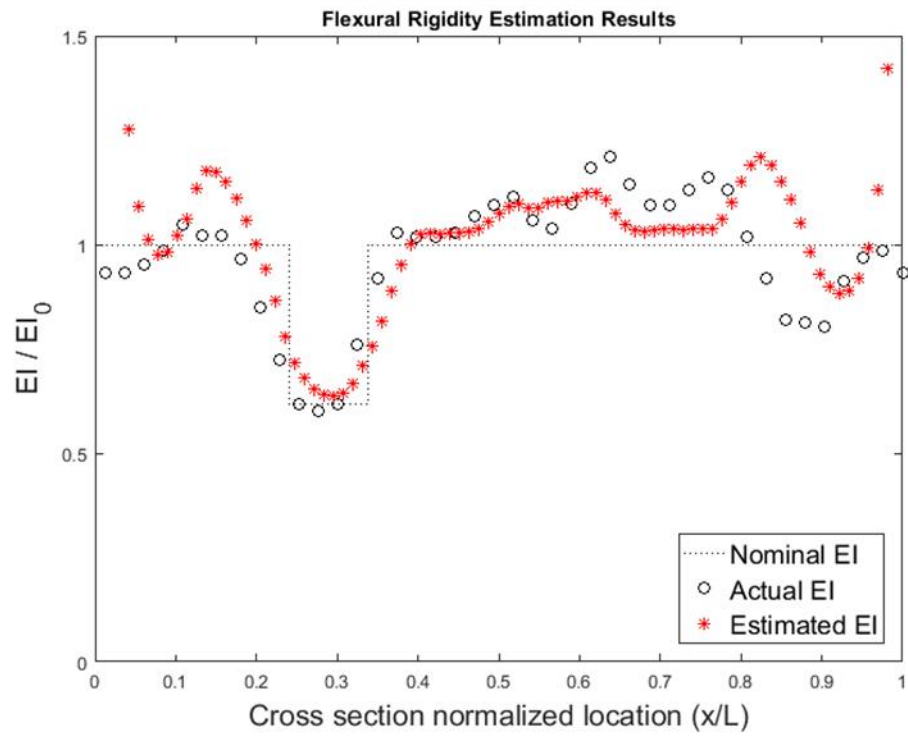
A cubic piecewise function with 82 pieces and $\lambda_{opt} = 0.0018$ is utilized for the curve fitting.

5.2.2 *Results and Discussion*

Figure 5.5a shows the results of RIL measurements and curve fitting to these measurements. By taking the second derivative of the resultant fitted curves and substituting into Eq. (3.1), the flexural rigidity of the specimen is estimated, and results are plotted in Figure 5.5b and labeled “Estimated EI”.



(a)



(b)

Figure 5.5: Experimental results, (a) Measured RILs and fitted curves, (b) Results of flexural rigidity estimation (FRE).

The geometry of this variable rectangular cross-section was measured using calipers with 1/100 mm accuracy at 5 mm increments. Assuming $E = 200$ GPa and using the

measured geometry, the flexural rigidity of this beam was calculated and plotted and labeled as “Actual EI” in Figure 5.5b. The nominal and actual flexural rigidities shown in Figure 5.5b differ due to small deviations in the specimen’s cross-section. Actual EI values are the reference values to which the estimated EI values from FRE results are compared.

Even in the presence of measurement noise and geometric deviations in intact sections of the specimen, the FRE method can quantify and localize the damage as a 40% reduction from 0.25 L to 0.34 L. Variations in the actual EI result from imperfections in the specimen; small variations in specimen thickness along the length can result in large departures from the nominal EI values. This result suggests that the FRE method can detect multiple reductions in EI that is caused by multiple damage locations.

5.3 Indeterminate Beam

5.3.1 Procedure

As an application of the presented framework to a statically indeterminate beam, a concentrated load of 28.2 N was applied at 6.35 mm increments along a 681 mm long propped cantilever. The bar is steel and has a nominal cross-section of 3.2 mm x 76.2 mm. Support conditions prevent vertical displacement at Point A and prevent translation and rotation at Point C. A severe reduction of 40% in flexural rigidity exists in the region from 0.25 L to 0.35 L from point A as depicted in Figure 5.6. A concentrated load traverses the entire span and beam rotations corresponding to each location of the concentrated load are measured at two stations, i.e., θ_A and θ_B . Rotations are measured using 2 cameras, 2 checkerboard targets, and a computer vision method for estimating structural rotations and displacements (Zeinali et al., 2017).

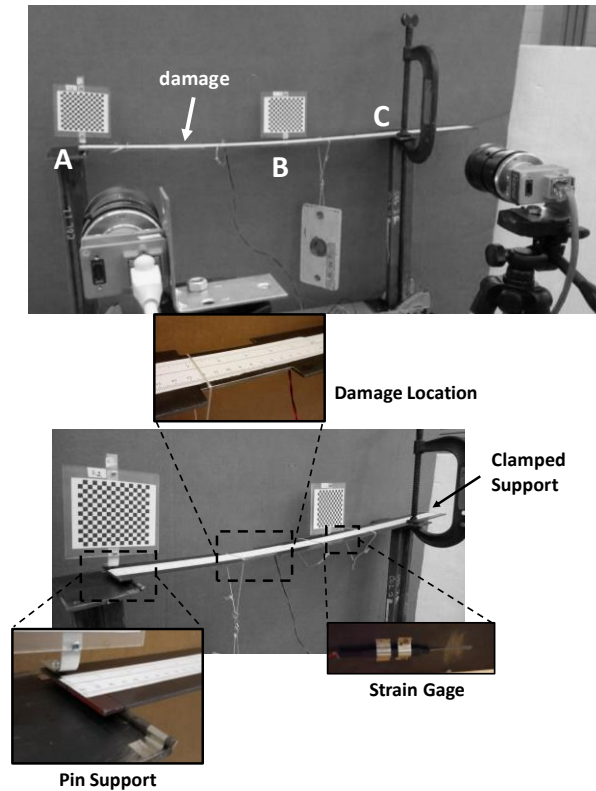


Figure 5.6: Experimental setup.

As stated before, the flexural rigidity estimate of this statically indeterminate system using the FRE method requires an additional measurement of internal deformation for each degree of redundancy. The need for this measurement arises because the moment $m(x)$ in Eq. (3.1), is also a function of the beam's flexural rigidity.

This system has one degree of redundancy; therefore, at least one strain measurement should be extracted as additional information with which to perform the FRE. In this example, the RIL at point A is measured and used in the FRE, so the moment $m(x)$ in Eq. (3.1) is the moment curve caused by a unit moment applied at point A, as the main system depicted in Figure 5.7. Using superposition of system-1 and system-2 in Figure 5.7 gives:

$$m(x) = m_{s_1}(x) + m_{s_2}(x) \quad (5.7)$$

Where, moment curve $m_{S_1}(x)$ is the moment curve of a simply supported beam under the effects of unit moment at point A and $m_{S_2}(x)$ is the moment curve of system-2. The only unknown in the right hand side of Eq. (5.7) is the magnitude of the moment for the system-2.

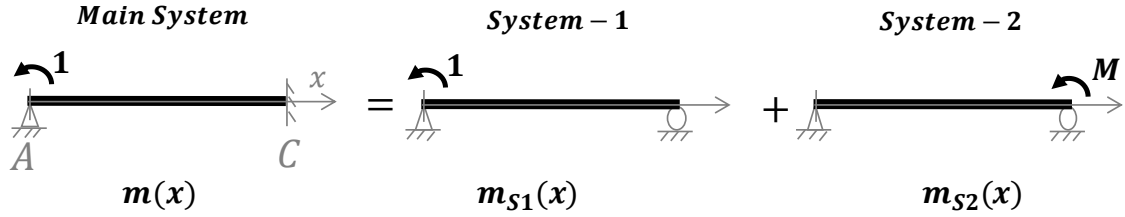


Figure 5.7: Superposition of statically-determinate systems for calculation of moment curve for the main statically-indeterminate system.

The strain measurement in this example is used for as additional information for calculation of the magnitude of the moment in system-2.

Assume that the value of the strain at location x_m is measured when unit load is at location ξ , i.e., $\varepsilon_{x_m}(\xi)$. Once the value of flexural rigidity is calculated at x_m , then, the value of moment influence line at this location can be calculated as:

$$M_{x_m}(\xi) = ES_{x_m} \times \varepsilon_{x_m}(\xi) \quad (5.8)$$

Where, ES_{x_m} represents the product of the section modulus and elastic modulus at location x_m . According to Figure 5.8,

$$M_{x_m}(\xi) = M_{x_m}^{S1}(\xi) + M_{x_m}^{S2}(\xi) \quad (5.9)$$

Where $M_{x_m}^{S1}(\xi)$ is the moment value at location x_m when a unit load is applied at ξ on system-1 and $M_{x_m}^{S2}(\xi)$ is the moment at x_m in system-2 in Figure 5.8. In this equation, $M_{x_m}^{S2}(\xi)$ is the only unknown and is a linear function of the moment at the clamped support, i.e. moment M in Figure 5.8. By solving this equation, the influence line of the moment at

the clamped support is calculated. The influence line of the moment at support C under the effect of the moving unit moment is the first derivative of the influence line of the moment that is calculated at this step. Once this curve is calculated, the value of the moment at clamped support in system-2 and the moment $m(x)$ can be calculated. The first derivative of the clamped moment influence line is calculated by fitting a smooth curve to the moment influence line at the clamped support under the effect of moving unit load.

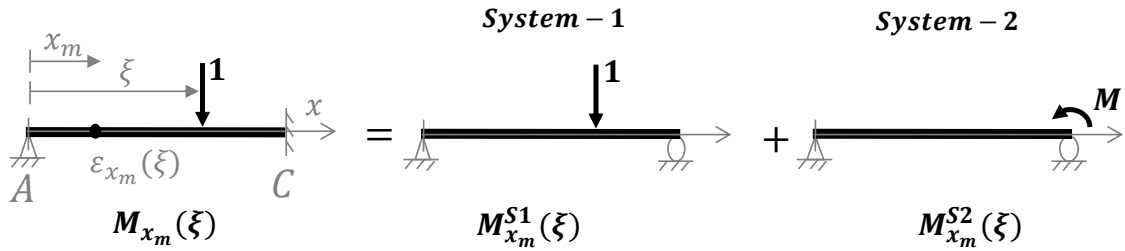


Figure 5.8: Superposition of statically-determinate systems for calculation of moment at the clamped support for the main statically-indeterminate system.

To improve the results of the experiment the weighted averages of three RILs are utilized as:

$$EI_{ave}(x) = f_A(x)EI_{\theta_A}(x) + f_B(x)EI_{\theta_B}(x) + f_C(x)EI_{\theta_C}(x) \quad (5.10)$$

Where shape functions f_A , f_B , and f_C are equal to unity at their own recording stations, i.e., at points A, B, and C, respectively, and equal to zero at the other two recording stations.

5.3.2 Verification of the Clamp Support

In this section, the assumption that the clamped support in the experimental setup is acting as a fixed support is investigated. A cantilever beam that is clamped using the same support apparatus as prior experiments is loaded. The deflection at the tip of the beam is measured and compared with the theoretical expected values. Figure 5.9 shows the experimental setup used. A narrow plate with 0.1205 in. thickness and 0.7505 in. width is

clamped at one end. A hook with 0.48 lbs. weight is put on six different points along the cantilever beam. The load is moved in 2 in. intervals. The corresponding deflection of the tip of the beam are 0.006, 0.022, 0.046, 0.072, 0.104, 0.139, where the corresponding theoretical values are 0.009, 0.025, 0.048, 0.076, 0.108, 0.142. Figure 5.10 plots the results of the experiment. It can be seen that the system response is very close to what in theory is expected from a cantilever beam, e.g., at the final load point, the difference between the measured deflection (0.139 in.) and the theoretical value (0.142 in.) is less than 2.1%. This means that the considered clamp, is adequate to create a fixed end.



Figure 5.9: Experimental setup for clamp support verification.

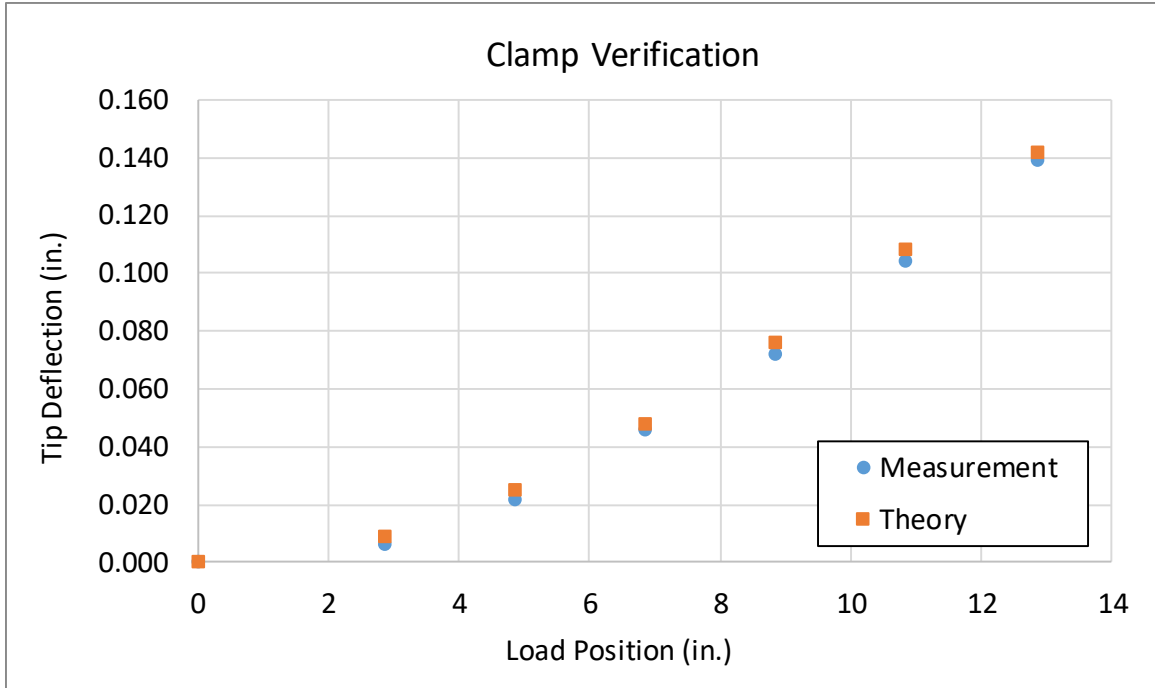
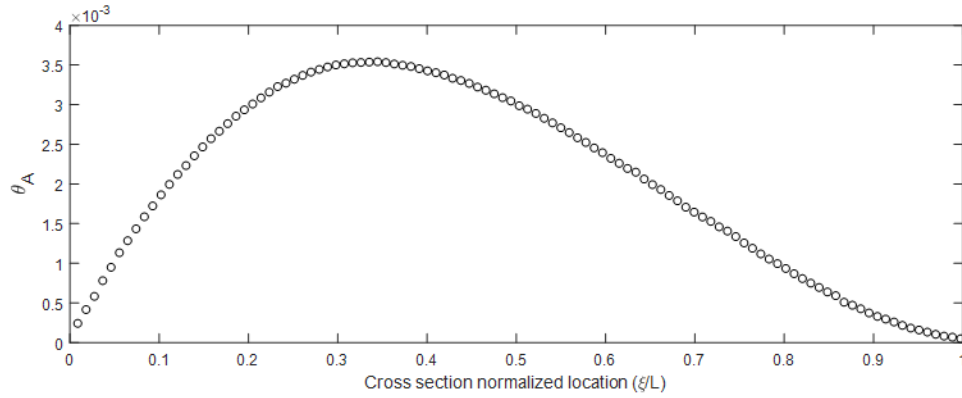


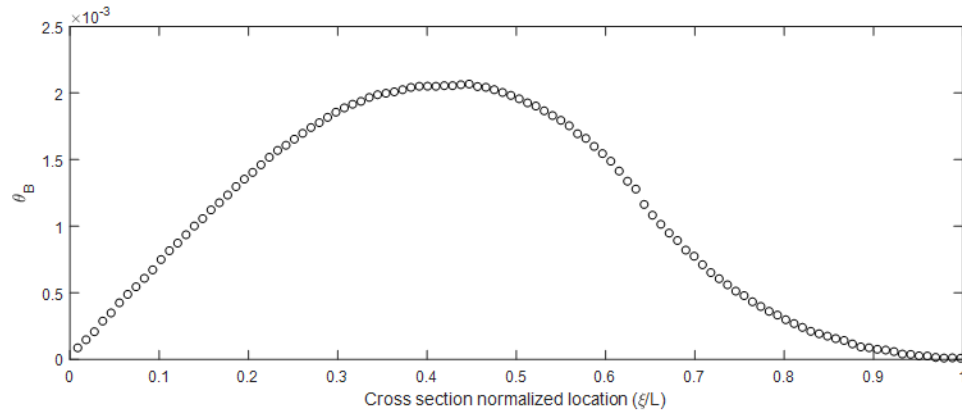
Figure 5.10: Tip deflection vs. load position for clamp verification.

5.3.3 Results and Discussion

By dividing the resultant rotation curves by the value of the load, the unit influence lines for rotations at locations A and B were calculated as shown in Figure 5.11. The NM and NS values for this experiment are 107 and 26, respectively.



(a)



(b)

Figure 5.11: Measured RILs, (a) at Point A, (b) at Point B.

Figure 5.12 presents the FRE results using TR along with nominal and actual values of flexural rigidity. The IMTR method, is also used to perform the FRE in this experiment. This method is described in detail by Zeinali and Story (2018). The actual EI values are calculated by using cross-section measurements taken with a caliper and assuming that the elastic modulus is equal to 200 GPa. These results are achieved by using the optimal values for the λ parameter in the TR method.

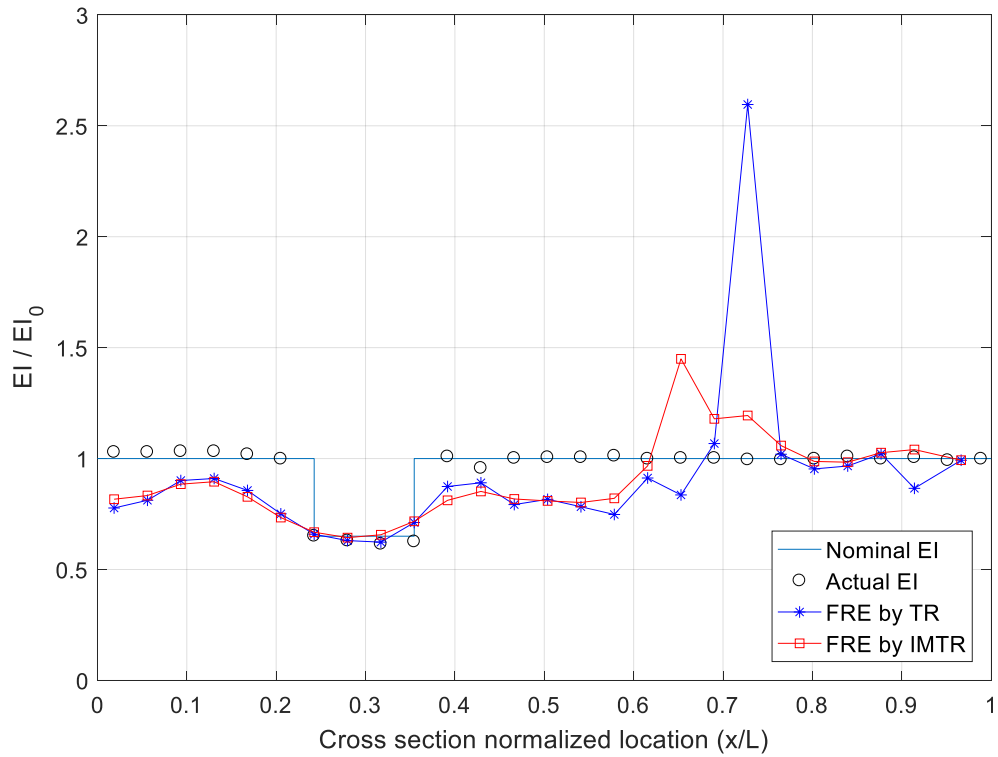
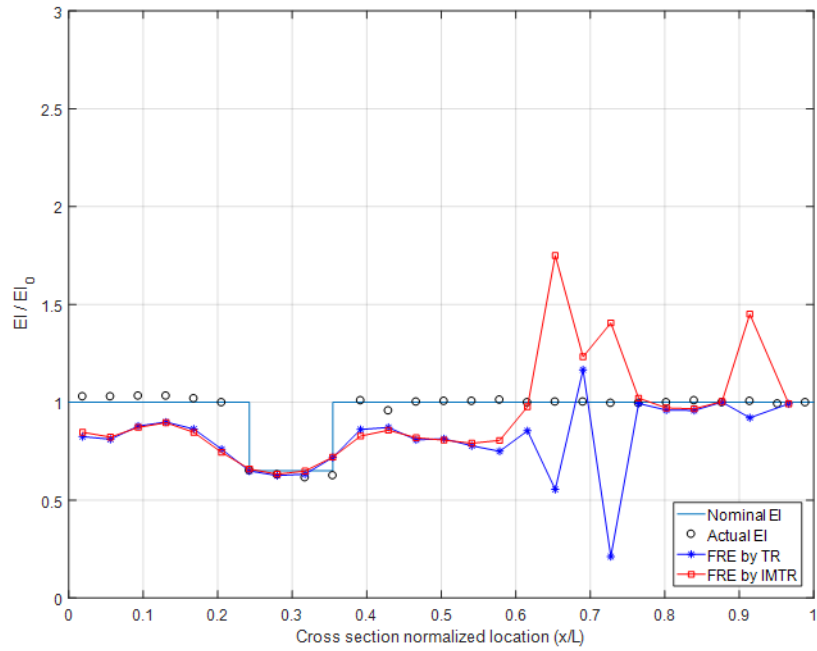
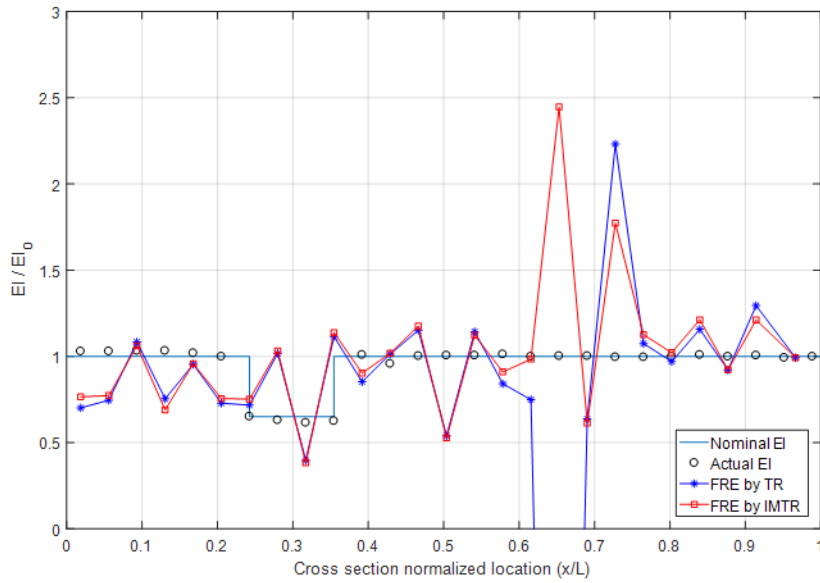


Figure 5.12: FRE results for propped cantilever laboratory experiment.

To illustrate the effects of number of measurements NM on FRE results, the same procedure is used with fewer load increments, i.e. smaller NM . Figure 5.13 presents the FRE results using TR for NM equal to 53 and 21.



(a)



(b)

Figure 5.13: F/EI results for propped cantilever experiment, (a) $NM = 5$, (b) $NM = 21$.

The results of the laboratory experiment shown in Figure 5.12 presents the prediction results using the TR method. Using Eq. (4.61) and the results from the TR method gives a

score of 0.11 for this method. Considering the score value and the resultant plot, indicates that the TR method performs adequately on both the damage localization and quantification of the damage severity with accuracy comparable to the scores presented in numerical simulations on the simply supported beams with varying damage. To achieve these results, RILs from points A, B, and C were weighted using the shape function approach in Eq (5.10). An increasing number of RIL (or DIL) measurement stations increases the accuracy of the method. The greatest deviation from the nominal EI, other than the damaged region, occurs in the region from $0.63L$ to $0.7L$; this is the location of the strain gage and, because of the size and stiffness of the strain gage to the specimen, the rigidity is affected significantly; the actual value of the rigidity is unknown at this location. In practice, even substantial measuring devices will not affect a full-scale structure to this degree. Additionally, the actual value of the rigidity at the location of the strain gage must be known for calculating the moment in Eq. (5.8).

Lastly, the number of measurements, NM , was investigated to assess the sensitivity of the accuracy of the method as fewer load increments were used. While accuracy decreased as NM was lowered below NS , using one half of the measurement increments still provided acceptable results in regions outside of the strain gage location. Using $1/5$ of the measurements produced inaccurate results. In practice, a significant amount of load placement locations may be required to accurately reconstruct the flexural rigidity and locate relatively small damage. This can be accommodated by either taking many measurements at small increments (e.g. 12"-18") along typical bridge span (e.g. 50').

5.4 Scale-Model Bridge

5.4.1 Procedure

To further test the techniques for flexural rigidity estimation (FRE) using rotation influence lines (RILs), the procedures used in Sections 5.1 and 5.3 were performed on a scale-model bridge. A simply-supported beam with a composite cross-section, consisting of two tube girders and a plate on top, was constructed and tested. The dimensions and material properties of the bridge are given in Table 5.1.

Table 5.1: Bridge dimensions and material properties.

Bridge			Plates			Girders		
Span Length	136	(in.)	Quantity	6		Quantity	2	
Width	48	(in.)	Length	24	(in.)	Spacing	36	(in.)
$I_{composite}$	2.18	(in. ⁴)	Width	48	(in.)	Length	136	(in.)
$I_{girders}$	0.63	(in. ⁴)	Thickness	0.25	(in.)	Width	1	(in.)
E	29000	(ksi)						
Thickness	0.12	(in.)						

The as-built plan and dimensions of the bridge are shown in Figure 5.14. A 131.5 lb. weight was passed over the bridge span with a resolution of 3 in. Support rotations were measured at all four support locations using cameras. To investigate the effect of the resolution of the rotation measurement tool on the output of the FRE method, a research grade inclinometer called CX1 sensor with a resolution of 0.00005 deg. is mounted at the location of the support A2.

Tests on three different scenarios were performed:

1. Intact bridge
2. Bridge Damage Case 01
3. Bridge Damage Case 02

Damage was applied by removing bolts connecting the bridge plates and girders which reduces the composite action of the system and thus reduces the rigidity. The panels from which bolts removed for each damage case are highlighted in Figure 5.15.

5.4.2 Verification Test

To evaluate the accuracy of the assumption that the structure is behaving as an Euler-Bernoulli beam, a static test is performed. In this test, a concentrated load is applied at the center of the beam, and the deflection of the mid-span before and after loading is measured at both sides of the beam. The corresponding deflection measurement at sides are 0.250 in. and 0.248 in. Hence, a 0.8% difference is observed in this measurement. Moreover, assuming that the experimental setup is an ideal simply-supported Euler-Bernoulli beam with a uniform composite flexural rigidity, the corresponding mid-span deflection is equal to 0.112 in. The same deflection measurement for a fully non-composite cross-section is equal to 0.389 in. It can be seen that the measured deflections are between these two limits. Hence, it is logical to assume that the structure is behaving as a Euler-Bernoulli beam.

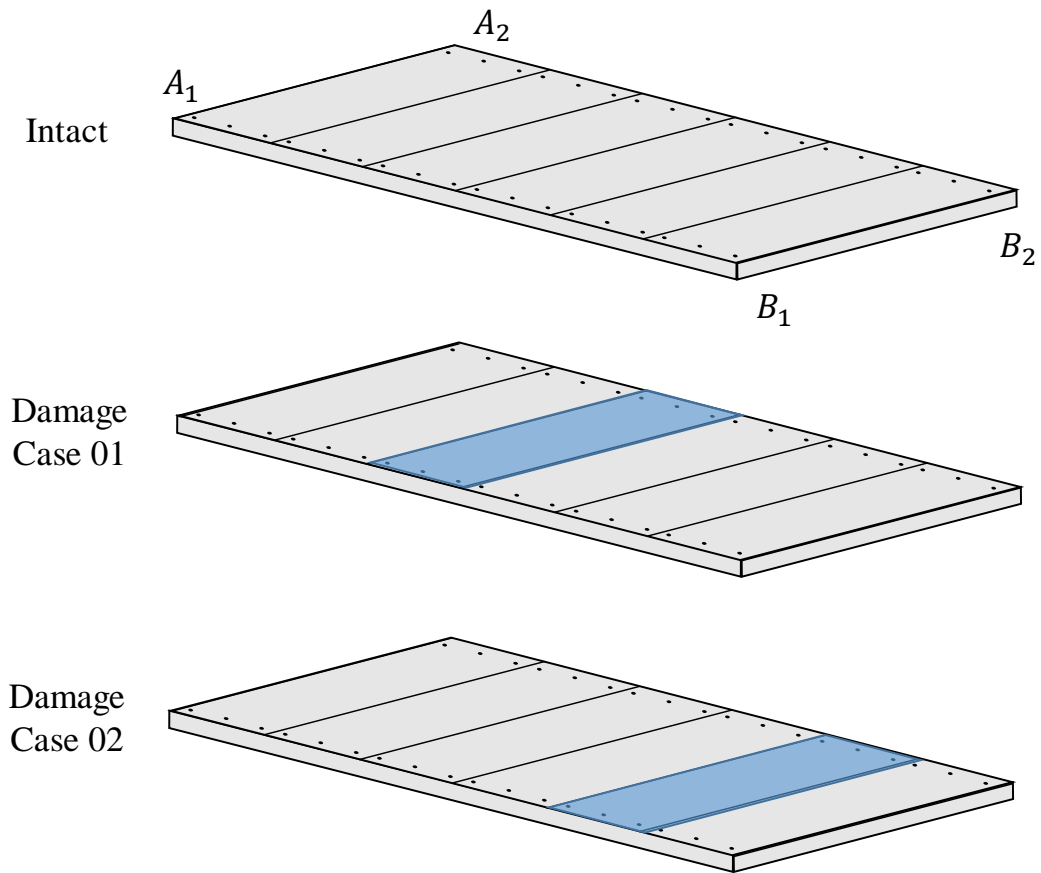


Figure 5.15 Considered damage case scenarios for scale-model experimental setup.

5.4.3 Results and Discussion

5.4.3.1 Damage Case 01

Figure 5.16 shows one series of representative measurements of rotation influence lines for test 01. The rest of the measurements are tabulated in the Appendix B.

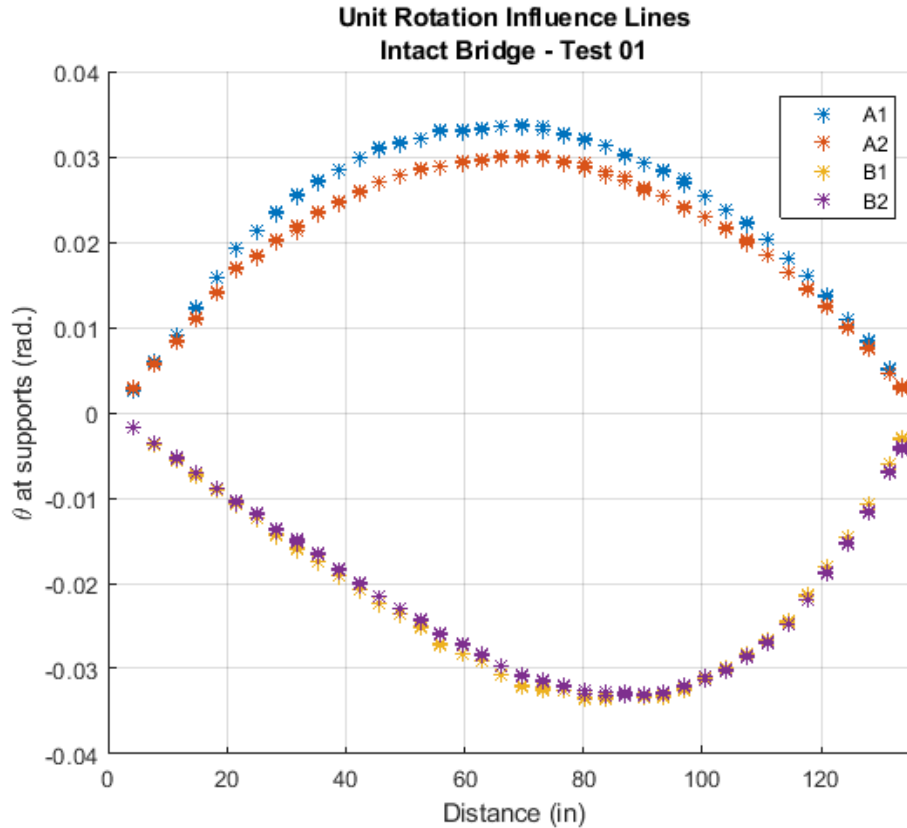


Figure 5.16: RIL for the intact bridge.

Rotations measured at points B1 and B2 were consistent throughout all tests; variations in rotations at points A1 and A2, were observed for each test. This indicates that some degree of two-dimensional interaction is presented in the experimental setup, close to the support A. This two-dimensional interaction violates the assumptions in the Euler-Bernoulli theory and the FRE will be negatively affected in this region.

After post-processing the measurements from the bridge, all the considered numerical methods are applied on the rotation measurements and presented in Figure 5.17a-c.

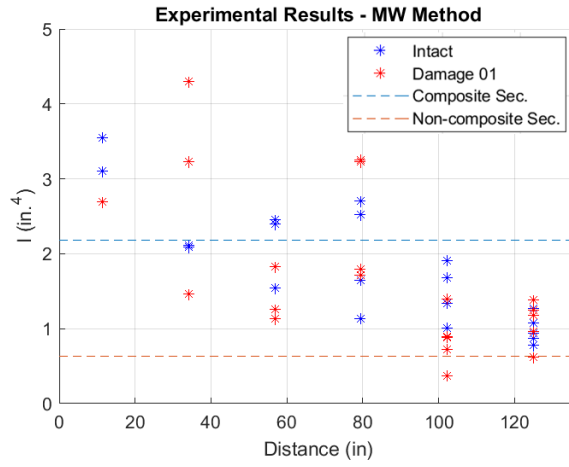
Lower performance of the MW algorithm on all tests indicates that the total level of noise from sensors, two-dimensional effects, local non-linear behavior (e.g. friction), and environmental factors (e.g. temperature) exceeds the appropriate level for the use of the

MW method. Both the TR and LSQ methods performed better; this trend follows the results from the analytical investigation presented in Chapter 4.

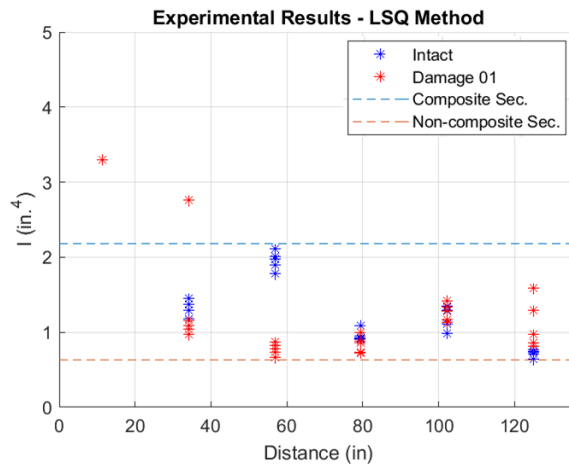
As illustrated in Figure 5.15, in damage case 01, the third panel from Support-A is damaged. In this scenario, no composite action exists at this panel, and the second moment of area should be close to what is anticipated from just two girders, i.e., $I = 0.63 \text{ in.}^4$. Comparing the FRE results from damaged beam with the intact beam from both methods shows the same expected trend. The prediction results in Figure 5.17 on the I value at the third panel shows significant drop compare to the results from the intact structure.

Comparing the corresponding plot from Figure 5.17b-c shows that the precision level of TR method is more than the LSQ method. This also shows that TR method is less sensitive to the existent noise level.

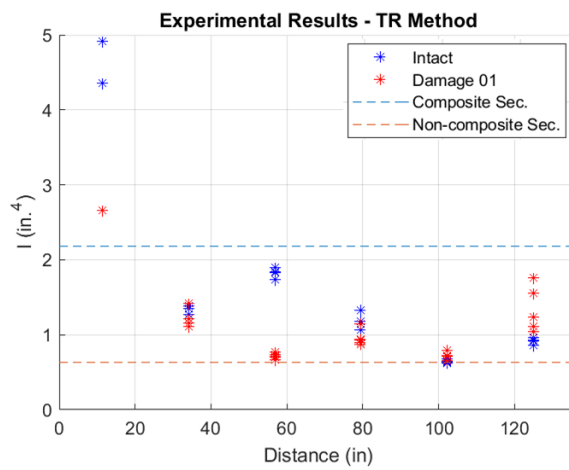
As expected, the FRE method is unable to make accurate or repeatable estimations near point A in the presence of significant two-dimensional effects.



(a)



(b)



(c)

Figure 5.17: Damaged Case Scenario 01. Experimental Results Comparisons (a) MW, (b) LSQ, (c) TR.

5.4.3.2 Damage Case 02

Figure 5.18a-c presents the FRE results for intact structure versus structure with damage case 02. Again, the MW method does not give a consistent results from test to test, on the same structure. Although, a good level of consistency is observed on TR and LSQ method, compared to MW method.

Both the TR and LSQ method are able to indicate a reduction on I at location of damage which is the second panel from support-B.

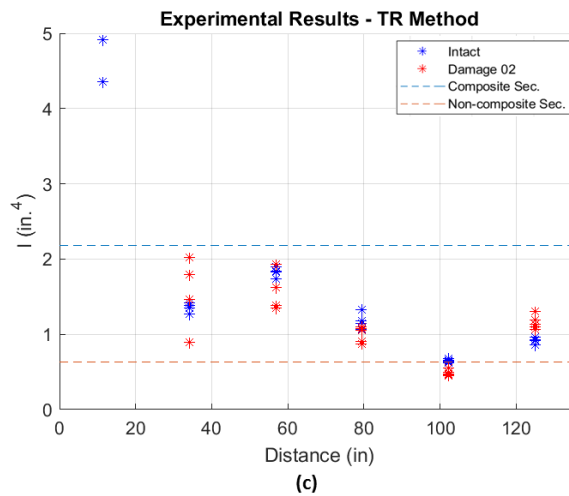
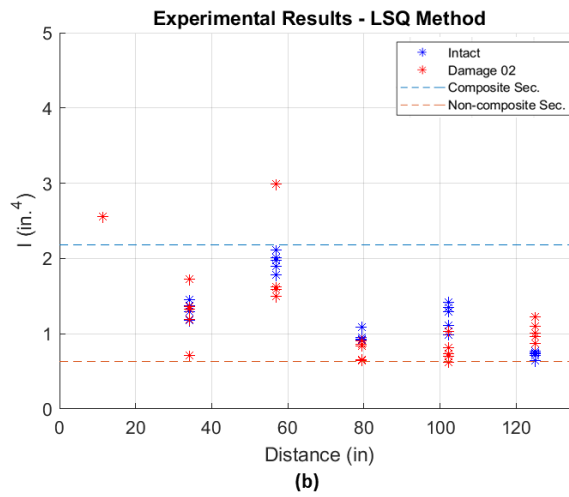
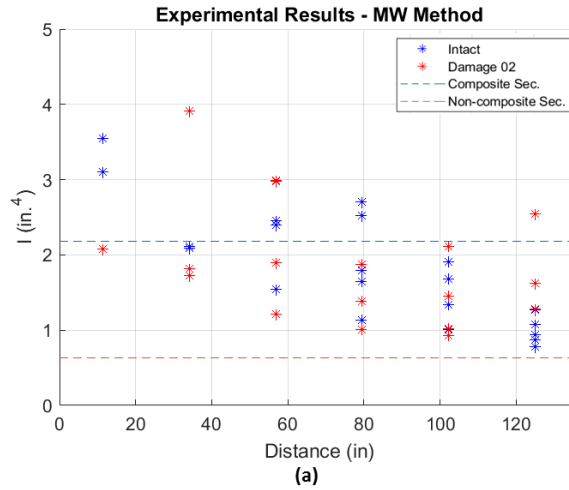


Figure 5.18 Damaged Case Scenario 02. Experimental Results Comparisons (a) MW, (b) LSQ, (c) TR.

CHAPTER 6

SUMMARY, CONCLUSIONS, AND CONTRIBUTIONS

6.1 Summary

This dissertation outlines a theoretical framework for the utilization of deformation influence lines calculated from a moving unit load for impairment detection on Euler-Bernoulli beams. The relationship between the second derivative of the deformation influence line (DIL or RIL) and the flexural rigidity of a beam is shown as the FRE equation. This novel formulation allows for both the location and quantification of damage directly from deformation data streams (i.e., deflection and rotation).

To overcome the challenges with noisy measurements, three numerical methods are proposed and compared, i.e., MW, LSQ, TR methods. Analytical studies have been presented to validate the FRE equation, in different combinations of noise level in the measurement and number of measurements.

A camera-based deformation measurement method is presented and studied to measure deflection or rotation influence lines in a non-contact manner. Ultimately, small and medium scaled tests were conducted and confirmed the applicability of the FRE method.

In this research study, mechanical theory, a computer-vision algorithm, and multiple numerical methods are integrated to demonstrate the feasibility of the FRE method.

6.2 Specific Conclusions and Contributions

The specific conclusions and contributions of this study are:

- The mechanical theory is developed that relates the influence line to the flexural rigidity for both determinant and indeterminate structures. Both the rotation and deflection influence lines can be used.
- Curve fitting methods presented in this study were able to overcome the problem noise in the measurement and give consistent and adequate results for the calculation of the second derivative in the FRE method, which is sensitive to the noisy measurement.
- TR and LSQ method are more stable and robust than the MW method against noisy measurements and lower numbers of measurements. This was confirmed by the experimental results.
- The non-contact, camera-based measurement technique using Zhang's camera calibration algorithm is presented and limits on the rotation and translation of the monitored target are established.

6.3 Future Work

Although assuming a Euler-Bernoulli structural behavior is a valid and practical assumption, it is also possible that, in some cases, the bridge structure behaves in a more complicated manner. So, a suggestion for future work is to study the same FRE framework based on influence surfaces. An extension of the current work to derivation of the FRE method based on dynamic influence surfaces is another suggestion for future work.

APPENDIX A
NOTATION LIST

α_x	Angular displacement at x of the modified beam under the effects of a virtual displacement
ε_l	Accuracy limit within which the second moment of area I is to be calculated
$\varepsilon_{l_{req.}}$	Required level of accuracy for the estimated flexural rigidity
$\varepsilon_{u''}$	Accuracy limit within which the second derivative is to be calculated
$\varepsilon_{x_m}(\xi)$	Strain at location x_m while a unit load is at location ξ
ξ	Distance of unit force from the beam left support
θ	Rotation of the beam
η	Regularization solution norm
λ	Regularization or smoothness parameter
λ_{opt}	Optimal value of the smoothing parameter
ρ	Least-mean-square solution norm
A	Camera intrinsic matrix
\mathbf{B}	Matrix of \mathbf{b}
$B_{i,j}$	Components of matrix \mathbf{B}
\mathbf{C}	Matrix of \mathbf{c}
$C_{i,j}$	Components of matrix \mathbf{C}
DOI	Degree of indeterminacy
E	Modulus of elasticity
EI	Flexural rigidity of the cross-section
EI_0	Nominal flexural rigidity
ES_{x_m}	Product of the section modulus and the elastic modulus at x_m

$EI_{ave.}$	Average of the flexural rigidity estimation
F	Function that projects the target spatial points onto the image plane
\hat{F}	Modified projection function
$I_{composite}$	Second moment of area for the composite section
$I_{girders}$	Second moment of area for the non-composite section
$I_{predicted}$	Predicted second moment of area for the system
I_{system}	Actual second moment of area for the system
J	Cost function for curve-fitting problem
K	Vector of distortion parameters
L	Matrix of the locations
L	Length of the beam
N	Number of images
NM	Number of measurements
NS	Number of segments
M	Beam internal moment caused by an externally-applied load
M_i	Number of points in each image
$M_{x_m}^{S_1}(\xi)$	Moment value at x_m while a unit load is at location ξ for system 1
P	3D point
P_C	Point in the camera coordinate system
P_W	Point in the world coordinate system
\tilde{R}_i	A matrix of R_i
R	Rotation matrix
R_i	Vertical reaction at support i
RE	Reprojection error
T	Translation vector
$X_{i,j}$	Target spatial points
X_c, Y_c, Z_c	Coordinates in the camera coordinate system
X_w, Y_w, Z_w	Coordinates in the world coordinate system

\mathbf{U}	Matrix of the u_i
a_i, b_i, c_i, d_i	Unknowns in the cubic curve fitting at segment- i
\mathbf{a}	Vector of a_i
\mathbf{b}	Vector of b_i
\mathbf{c}	Vector of c_i
d_x	Tangential distortion due to imperfect centering of the lens components
f_A, f_B	Wight for the averaging
f_x, f_y	Effective focal length in x, and y directions
k_1, k_2, k_3	Radial distortion amplification
$\tilde{\mathbf{m}}$	A matrix of m
$\tilde{\mathbf{m}}_i$	A matrix of m_i
$\tilde{\mathbf{m}}_{UL}$	A matrix of m_{UL}
m	Resultant internal moment caused by a unit load
$m_{\theta_A}, m_{\theta_B}$	Moment diagram caused by a unit moment at support-A, support-B
m_i	Moment that is caused by a unit load that is applied on a simply-supported beam at the interior support i
m_{UL}	Moment that is caused by a unit load applied at a distance x_0 on a simply-supported beam
$px + q$	Parametric format of the linear moment $m(x)$
r	Square root of $(x_n^2 + y_n^2)$
u, v	Pixel coordinate components
u_A	Deflection of point A
u_{x_A}''	Second derivative of the rotation or deflection influence line at point x
u_0, v_0	Principal point coordinate in pixel units
u_i	Fitted curve to the noisy influence line in segment i
u_{LSQ}	Fitted curve for the least-mean square error (LSQ) method
u_{MW}	Fitted curve for the moving window method
u_{TR}	Fitted curve for the Tikhonov Regularization method
w_{MW_i}	Parameters that define the linear relation between the u_i and the u_i'' for MW method

w_{LSQ_i}	Parameters that define the linear relation between the u_i and the u_i'' for LSQ method
x_d, y_d	Distorted pixel coordinate
$x_{i,j}$	Image plane
x_n, y_n	Normalized pixel coordinates
y	Vertical deflection at point x when unit load is at location ξ
$y_{M.B.}$	Deflection curve of the modified beam under the effects of a virtual displacement

REFERENCES

- ASCE. (2017). *2017 Infrastructure Report Card*. American Society of Civil Engineers.
<https://doi.org/10.1017/CBO9781107415324.004>
- Bakeer, T. (2016). Assessment the stability of masonry walls by the transfer-matrix method. *Engineering Structures*, *110*, 1–20.
<https://doi.org/10.1016/j.engstruct.2015.11.052>
- Bernal, D. (2014). Damage Localization from the Image of Changes in Flexibility. *Conference Proceedings of the Society for Experimental Mechanics Series*, *45(7)*, 369–375. https://doi.org/10.1007/978-1-4614-6585-0_34
- Bouguet, J. Y. (2000). Matlab Camera Calibration Toolbox.
- Brown, D. C. (1966). Decentering distortion of lenses. *Photogrammetric Engineering and Remote Sensing*, *32(3)*, 444–462.
- Burger, W. (2016). *Zhang's Camera Calibration Algorithm: In-Depth Tutorial and Implementation*. Technical Report HGB16-05. Hagenberg, Austria.
<https://doi.org/10.13140/RG.2.1.1166.1688>
- Busca, G., Cigada, A., Mazzoleni, P., & Zappa, E. (2014). Vibration Monitoring of Multiple Bridge Points by Means of a Unique Vision-Based Measuring System. *Experimental Mechanics*, *54(2)*, 255–271. [https://doi.org/10.1007/s11340-013-9784-](https://doi.org/10.1007/s11340-013-9784-8)

- Catbas, F. N., Lenett, M. S., Aktan, A. E., Brown, D. L., Helmicki, A. J., & Hunt, V. (1998). Damage detection and condition assessment of Seymour bridge. In *Proceedings of the 16th International Modal Analysis Conference* (Vol. 3243, p. 1694).
- Catbas, F. N., Zaurin, R., Gul, M., & Gokce, H. B. (2012). Sensor Networks, Computer Imaging, and Unit Influence Lines for Structural Health Monitoring: Case Study for Bridge Load Rating. *Journal of Bridge Engineering*, 17(4), 662–670. [https://doi.org/10.1061/\(ASCE\)BE.1943-5592.0000288](https://doi.org/10.1061/(ASCE)BE.1943-5592.0000288)
- Catbas, F. N., Zaurin, R., Susoy, M., & Gul, M. (2007). Integrative Information System Design for Florida Department of Transportation, (June).
- Chang, C. C., & Ji, Y. F. (2007). Flexible Videogrammetric Technique for Three-Dimensional Structural Vibration Measurement. *Journal of Engineering Mechanics*, 133(6), 656–664. [https://doi.org/10.1061/\(ASCE\)0733-9399\(2007\)133:6\(656\)](https://doi.org/10.1061/(ASCE)0733-9399(2007)133:6(656))
- Chang, C. C., & Xiao, X. H. (2010). Three-Dimensional Structural Translation and Rotation Measurement Using Monocular Videogrammetry. *Journal of Engineering Mechanics*, 136(7), 840–848.
- Chang, P. C., Flatau, A., & Liu, S. C. (2003). Review paper: Health monitoring of civil infrastructure. *Structural Health Monitoring*, 2(3), 257–267. <https://doi.org/10.1177/147592170303036169>
- Chen, C. C., Wu, W. H., Tseng, H. Z., Chen, C. H., & Lai, G. (2015). Application of digital photogrammetry techniques in identifying the mode shape ratios of stay cables with multiple camcorders. *Measurement: Journal of the International Measurement Confederation*, 75, 134–146. <https://doi.org/10.1016/j.measurement.2015.07.037>
- Chen, J. G., Davis, A., Wadwha, N., Fredo, D., Freeman, W. T., & Buyukozturk, O. (2017).

- Video-Based Vibration Measurement for Civil Infrastructure Applications. *Journal of Infrastructure Systems*, 23(3), B4016013. [https://doi.org/10.1061/\(ASCE\)IS.1943-555X.0000348](https://doi.org/10.1061/(ASCE)IS.1943-555X.0000348).
- Chen, Z.-W., Zhu, S., Xu, Y.-L., Li, Q., & Cai, Q.-L. (2015). Damage Detection in Long Suspension Bridges Using Stress Influence Lines. *Journal of Bridge Engineering*, 20(3), 05014013. [https://doi.org/10.1061/\(ASCE\)BE.1943-5592.0000681](https://doi.org/10.1061/(ASCE)BE.1943-5592.0000681)
- Choi, H. S., Cheung, J. H., Kim, S. H., & Ahn, J. H. (2011). Structural dynamic displacement vision system using digital image processing. *NDT and E International*, 44(7), 597–608. <https://doi.org/10.1016/j.ndteint.2011.06.003>
- Clough, R. W., & Penzien, J. (1975). *Dynamics of Structures*. New York, NY: McGraw-Hill.
- Cross, E. J., Koo, K. Y., Brownjohn, J. M. W., & Worden, K. (2013). Long-term monitoring and data analysis of the Tamar Bridge. *Mechanical Systems and Signal Processing*, 35(1–2), 16–34. <https://doi.org/10.1016/j.ymsp.2012.08.026>
- Das, S., Saha, P., & Patro, S. K. (2016). Vibration-based damage detection techniques used for health monitoring of structures: a review. *Journal of Civil Structural Health Monitoring*, 6(3), 477–507. <https://doi.org/10.1007/s13349-016-0168-5>
- Doebling, S. W., Farrar, C. R., & Prime, M. B. (1997). *A Summary Review of Vibration-Based Damage Identification Methods*. Technical report, Los Alamos National Laboratory.
- Dzunic, Z., Chen, J. G., Mobahi, H., Büyüköztürk, O., & Fisher, J. W. (2017). A Bayesian state-space approach for damage detection and classification. *Mechanical Systems and Signal Processing*, 96, 239–259. <https://doi.org/10.1016/j.ymsp.2017.03.043>

- Engl, H. W., Hanke, M., & Neubauer, A. (1996). *Regularization of inverse problems*. Dordrecht, The Netherlands: Kluwer Academic Publishers.
- Fan, W., & Qiao, P. (2011). Vibration-based damage identification methods: A review and comparative study. *Structural Health Monitoring*, *10*(1), 83–111. <https://doi.org/10.1177/1475921710365419>
- Feng, D., & Feng, M. Q. (2016). Vision-based multipoint displacement measurement for structural health monitoring. *Structural Control and Health Monitoring*, *23*, 876–890. <https://doi.org/10.1002/stc.1819>
- Feng, D., & Feng, M. Q. (2017). Experimental validation of cost-effective vision-based structural health monitoring. *Mechanical Systems and Signal Processing*, *88*(November 2016), 199–211. <https://doi.org/10.1016/j.ymssp.2016.11.021>
- Feng, D., Feng, M. Q., Ozer, E., & Fukuda, Y. (2015). A vision-based sensor for noncontact structural displacement measurement. *Sensors*, *15*, 16557–16575. <https://doi.org/10.3390/s150716557>
- Feng, D., Scarangelo, T., Feng, M. Q., & Ye, Q. (2017). Cable tension force estimate using novel noncontact vision-based sensor. *Measurement: Journal of the International Measurement Confederation*, *99*, 44–52. <https://doi.org/10.1016/j.measurement.2016.12.020>
- Ferrer, B., Mas, D., García-Santos, J. I., & Luzi, G. (2016). Parametric Study of the Errors Obtained from the Measurement of the Oscillating Movement of a Bridge Using Image Processing. *Journal of Nondestructive Evaluation*, *35*(4), 1–10. <https://doi.org/10.1007/s10921-016-0372-6>
- Franco, J. M., Mayag, B. M., Marulanda, J., & Thomson, P. (2017). Static and dynamic

- displacement measurements of structural elements using low cost RGB-D cameras. *Engineering Structures*, 153, 97–105. <https://doi.org/10.1016/j.engstruct.2017.10.018>
- Fukuda, Y., Feng, M. Q., & Shinozuka, M. (2010). Cost-effective vision-based system for monitoring dynamic response of civil engineering structures. *Structural Control and Health Monitoring*, 17(8), 918–936. <https://doi.org/10.1002/stc.360>
- Golub, G. H., Heath, M., & Wahba, G. (1979). Generalized cross-validation as a method for choosing a good ridge parameter. *Technometrics*, 21(2), 215–223. <https://doi.org/10.1080/00401706.1979.10489751>
- Hansen, P. C. (1992). Analysis of discrete ill-posed problems by means of the L-curve. *SIAM Review*, 34(4), 561–580.
- Hansen, P. C. (1998). *Rank-Deficient and Discrete Ill-Posed Problems: Numerical Aspects of Linear Inversion*. Philadelphia, PA: Society for Industrial and Applied Mathematics. <https://doi.org/10.1137/1.9780898719697>
- Hansen, P. C., & O’Leary, D. P. (1993). The use of the L-curve in the regularization of discrete ill-posed problems. *SIAM J. Sci. Comput.*, 14(6), 1487–1503.
- Hardle, W. (1991). *Smoothing Techniques with Implementation in S*. New York, NY: Springer-Verlag.
- Heikkila, J. (2000). Geometric Camera Calibration Using Circular Control Points. *IEEE Transactions on Pattern Analysis and Machine Intelligence*, 22(10), 1066–1077.
- Heikkila, J., & Silven, O. (1997). A four-step camera calibration procedure with implicit image correction. In *Proceedings of IEEE Computer Society Conference on Computer Vision and Pattern Recognition (CVPR-97)* (pp. 1106–1112). <https://doi.org/10.1109/CVPR.1997.609468>

- Hu, H., Liang, J., Xiao, Z. Z., Tang, Z. Z., Asundi, A. K., & Wang, Y. X. (2012). A four-camera videogrammetric system for 3-D motion measurement of deformable object. *Optics and Lasers in Engineering*, 50(5), 800–811. <https://doi.org/10.1016/j.optlaseng.2011.12.011>
- Jain, R., Kasturi, R., & Schunck, B. G. (1995). *Machine Vision* (5th ed.). New York, NY: McGraw-Hill.
- Kohut, P., Holak, K., & Martowicz, A. (2012). An uncertainty propagation in developed vision based measurement system aided by numerical and experimental tests. *Journal of Theoretical and Applied Mechanics*, 50(4), 1049–1061.
- Li, X. Y., & Law, S. S. (2010). Adaptive Tikhonov regularization for damage detection based on nonlinear model updating. *Mechanical Systems and Signal Processing*, 24(6), 1646–1664. <https://doi.org/10.1016/j.ymsp.2010.02.006>
- Mathworks. (2017). Global Optimization Toolbox: User's Guide (r2017b). Retrieved November 30, 2017, from http://www.mathworks.com/help/pdf_doc/gads/gads_tb.pdf
- Mazzoni, S., McKenna, F., Scott, M. H., & Fenves, G. L. (2006). *OpenSees command language manual*.
- Oh, B. K., Hwang, J. W., Kim, Y., Cho, T., & Park, H. S. (2015). Vision-based system identification technique for building structures using a motion capture system. *Journal of Sound and Vibration*, 356, 72–85. <https://doi.org/10.1016/j.jsv.2015.07.011>
- Pereverzev, S., & Schock, E. (2000). Morozov's discrepancy principle for Tikhonov regularization of severely ill-posed problems in finite-dimensional subspaces.

- Numerical Functional Analysis and Optimization*, 21(7–8), 901–916.
- Ranjbar, Z. (2010). Numerical Solution of Ill-posed Cauchy Problems for Parabolic Equations, (1300). <https://doi.org/10.1177/0148607114528981>
- Ribeiro, D., Calçada, R., Ferreira, J., & Martins, T. (2014). Non-contact measurement of the dynamic displacement of railway bridges using an advanced video-based system. *Engineering Structures*, 75, 164–180. <https://doi.org/10.1016/j.engstruct.2014.04.051>
- Robson, S., MacDonald, L., Kyle, S., & Shortis, M. R. (2016). Close range calibration of long focal length lenses in a changing environment. *International Archives of the Photogrammetry, Remote Sensing and Spatial Information Sciences - ISPRS Archives, XLI-B5*, 115–122. <https://doi.org/10.5194/isprsarchives-XLI-B5-115-2016>
- Rytter, A. (1993). *Vibration based inspection of civil engineering structures*. Aalborg University, Aalborg, Denmark.
- Santini-Bell, E., Brogan, P. A., Lefebvre, P. J., Peddle, J., Brenner, B., & Sanayei, M. (2010). *Digital Imaging for Bridge Deflection Measurement of a Steel Girder Composit Bridge*. Washington D.C.
- Seo, J., Hu, J. W., & Lee, J. (2016). Summary Review of Structural Health Monitoring Applications for Highway Bridges. *J. Perform. Constr. Facil.*, 30(4), 04015072. [https://doi.org/10.1061/\(ASCE\)CF.1943-5509.0000824](https://doi.org/10.1061/(ASCE)CF.1943-5509.0000824)
- Shan, B., Wang, L., Huo, X., Yuan, W., & Xue, Z. (2016). A Bridge Deflection Monitoring System Based on CCD. *Advances in Materials Science and Engineering*, 2016. <https://doi.org/10.1155/2016/4857373>
- Shan, B., Zheng, S., & Ou, J. (2015). Free vibration monitoring experiment of a stayed-cable model based on stereovision. *Measurement: Journal of the International*

Measurement *Confederation*, 76, 228–239.
<https://doi.org/10.1016/j.measurement.2015.08.025>

Simonoff, J. S. (1996). *Smoothing methods in statistics*. New York, NY: Springer-Verlag.

Sładek, J., Ostrowska, K., Kohut, P., Holak, K., Gąska, A., & Uhl, T. (2013). Development of a vision based deflection measurement system and its accuracy assessment. *Measurement: Journal of the International Measurement Confederation*, 46(3), 1237–1249. <https://doi.org/10.1016/j.measurement.2012.10.021>

Sohn, H., Farrar, C. R., Hemez, F., & Czarnecki, J. (2002). *A Review of Structural Health Monitoring Literature 1996 – 2001*. Technical report, Los Alamos National Laboratory.

Stephen, N. G. (2009). Repetitive beam-like structures: Distributed loading and intermediate support. *International Journal of Solids and Structures*, 46(20), 3664–3668. <https://doi.org/10.1016/j.ijsolstr.2009.06.016>

Stimac Grandic, I. (2014). Influence of sampling interval on deflection-influence-line-based damage detection in beams. In *Proceedings of the 5th International Conference on Civil Engineering Science and Practice* (pp. 355–361). Bellingham, WA. <https://doi.org/10.5937/jaes12-5668>

Stimac, I., Grandic, D., & Bjelnovic, A. (2011). Comparison of Techniques for Damage Identification Based on Influence Line Approach. *Machines, Technologies, Materials*, 7, 9–13.

Stimac, I., Mihanovic, A., & Kozar, I. (2006). Damage Detection From Analysis of Displacement Influence Lines. In *Structural Engineering Conferences: International Conference on Bridges* (pp. 1001–1008). Dubrovnik, Croatia.

- Story, B. A. (2012). *Structural impairment detection using arrays of competitive artificial neural networks*. Texas A&M University, College Station, TX.
- Story, B. A., & Fry, G. T. (2014a). A Structural Impairment Detection System Using Competitive Arrays of Artificial Neural Networks. *Computer-Aided Civil and Infrastructure Engineering*, 29, 180–190. Retrieved from <http://doi.wiley.com/10.1111/mice.12040>
- Story, B. A., & Fry, G. T. (2014b). Methodology for Designing Diagnostic Data Streams for Use in a Structural Impairment Detection System. *Journal of Bridge Engineering*, 19(4), 04013020. [https://doi.org/10.1061/\(ASCE\)BE.1943-5592.0000556](https://doi.org/10.1061/(ASCE)BE.1943-5592.0000556)
- Story, B. A., & Fry, G. T. (2014c). Methodology for Designing Diagnostic Data Streams for Use in a Structural Impairment Detection System. *Journal of Bridge Engineering*, 19(4).
- Sun, Z., Nagayama, T., & Fujino, Y. (2016). Minimizing noise effect in curvature-based damage detection. *Journal of Civil Structural Health Monitoring*, 6(2), 255–264. <https://doi.org/10.1007/s13349-016-0163-x>
- Tikhonov, A. N., Goncharsky, A. V., Stempanov, V. V., & Yagola, A. G. (1995). *Numerical methods for the solution of ill-posed problems*. Boston, MA: Kluwer Academic Publishers.
- Tsai, R. Y. (1986). An efficient and accurate camera calibration technique for 3D machine vision. In *Proc. of Comp. Vis. Patt. Recog.* (pp. 364–374).
- Turer, A. (2000). *Conditional evaluation and load rating of steel stringer highway bridges using field calibrated 2D grid and 3D FE models*. University of Cincinnati, Cincinnati, OH.

- Turer, A., Levi, A., & Aktan, A. E. (1998). *Instrumentation proof-testing and monitoring of three reinforced concrete deck-on-steel girder bridges prior to, during, and after superload*. Cincinnati, OH.
- Wang, Y., & Liu, X. (2014). Beam damage localization method considering random uncertainty using mid-span displacement data. In *Sustainable Development of Critical Infrastructure: Proceedings of the 2014 International Conference on Sustainable Development of Critical Infrastructure*. Shanghai, China.
- Worden, K., & Dulieu-Barton, J. M. (2004). An Overview of Intelligent Fault Detection in Systems and Structures. *Structural Health Monitoring*, 3(1), 85–98. <https://doi.org/10.1177/1475921704041866>
- Yang, Z. B., Radzienski, M., Kudela, P., & Ostachowicz, W. (2017a). Damage detection in beam-like composite structures via Chebyshev pseudo spectral modal curvature. *Composite Structures*, 168, 1–12. <https://doi.org/10.1016/j.compstruct.2017.01.087>
- Yang, Z. B., Radzienski, M., Kudela, P., & Ostachowicz, W. (2017b). Fourier spectral-based modal curvature analysis and its application to damage detection in beams. *Mechanical Systems and Signal Processing*, 84, 763–781. <https://doi.org/10.1016/j.ymsp.2016.07.005>
- Ye, X. W., Dong, C. Z., & Liu, T. (2016). A Review of Machine Vision-Based Structural Health Monitoring: Methodologies and Applications. *Journal of Sensors*, 2016. <https://doi.org/10.4149/gpb-2016016>
- Zaurin, R., & Catbas, F. N. (2010). Integration of computer imaging and sensor data for structural health monitoring of bridges. *Smart Materials and Structures*, 19(1). <https://doi.org/10.1088/0964-1726/19/1/015019>

- Zaurin, R., & Catbas, F. N. (2011). Structural health monitoring using video stream, influence lines, and statistical analysis. *Structural Health Monitoring*, 10(3), 309–332. <https://doi.org/10.1177/1475921710373290>
- Zaurin, R., Khuc, T., & Catbas, F. N. (2015). Hybrid Sensor-Camera Monitoring for Damage Detection: Case Study of a Real Bridge. *Journal of Bridge Engineering*, 21(6), 1–27. [https://doi.org/10.1061/\(ASCE\)BE.1943](https://doi.org/10.1061/(ASCE)BE.1943)
- Zeinali, Y., Li, Y., Rajan, D., & Story, B. (2017). Accurate Structural Dynamic Response Monitoring of Multiple Structures using One CCD Camera and a Novel Targets Configuration. In *Proceedings of the 11th International Workshop on Structural Health Monitoring* (pp. 12–14). Palo Alto, CA. <https://doi.org/10.12783/shm2017/14219>
- Zeinali, Y., & Story, B. (2016). Structural Impairment Detection Using Deep Counter Propagation Neural Networks. *Procedia Engineering*, 145(May), 868–875. <https://doi.org/10.1016/j.proeng.2016.04.113>
- Zeinali, Y., & Story, B. A. (2017). Framework for Flexural Rigidity Estimation in Euler-Bernoulli Beams Using Deformation Influence Lines. *Infrastructures*, 2(4), 23. <https://doi.org/10.3390/infrastructures2040023>
- Zeinali, Y., & Story, B. A. (2018). Impairment localization and quantification using noisy static deformation influence lines and Iterative Multi-parameter Tikhonov Regularization. *Mechanical Systems and Signal Processing*, 109, 399–419. <https://doi.org/10.1016/j.ymsp.2018.02.036>
- Zhang, W., Li, J., Hao, H., & Ma, H. (2017). Damage detection in bridge structures under moving loads with phase trajectory change of multi-type vibration measurements.

Mechanical Systems and Signal Processing, 87, 410–425.

<https://doi.org/10.1016/j.ymssp.2016.10.035>

Zhang, Z. (2000). A Flexible New Technique for Camera Calibration. *IEEE Transactions on Pattern Analysis and Machine Intelligence*, 22(11), 1330–1334.